

Electromagnetic induction in the icy satellites of Uranus

Christopher S. Arridge (1) and Joseph W. B. Eggington (1,2)

1. Department of Physics, Lancaster University, Bailrigg, Lancaster, LA1 4YB, UK; c.arridge@lancaster.ac.uk

2. Space and Atmospheric Physics, The Blackett Laboratory, Imperial College, South Kensington, London, SW7 2AZ, UK.

Abstract

The discovery of subsurface oceans in the outer solar system has transformed our perspective of ice worlds and has led to consideration of their potential habitability. The detection and detailed characterisation of induced magnetic fields due to these subsurface oceans provides a unique ability to passively sound the conducting interior of such planetary bodies. In this paper we consider the potential detectability of subsurface oceans via induced magnetic fields at the main satellites of Uranus. We construct a simple model for Uranus' magnetospheric magnetic field and use it to generate synthetic time series which are analysed to determine the significant amplitudes and periods of the inducing field. The spectra not only contain main driving periods at the synodic and orbital periods of the satellites, but also a rich spectrum from the mixing of signals due to asymmetries in the uranian planetary system. We use an induction model to determine the amplitude of the response from subsurface oceans and find weak but potentially-detectable ocean responses at Miranda, Oberon and Titania, but did not explore this in detail for Ariel and Umbriel. Detection of an ocean at Oberon is complicated by intervals that Oberon will spend outside the magnetosphere at equinox but we find that flybys of Titania with a closest approach altitude of 200 km would enable the detection of subsurface oceans. We comment on the implications for future mission and instrument design.

1. Introduction

1.1 Ocean worlds

Evidence of subsurface liquid oceans beneath the frozen ice crusts of the icy satellites of Jupiter and Saturn has changed our perspective of small icy worlds in the outer solar system; these worlds are not inert. Furthermore, the possibility of extant microbial life in their oceans has forced us to reconsider the meaning of planetary 'habitability' throughout the solar system and beyond (e.g., Lazcano and Hand, 2012). Measurements of Europa's gravity field pointed towards a three-shell model consisting of an H_2O layer overlying a silicate mantle and metallic core. Although the state of the H_2O layer was unknown, surface geomorphology, including cryovolcanic features, chaos terrain, topography and global tectonics, argued for a liquid subsurface ocean (Anderson et al., 1998; Pappalardo et al., 1999).

One of the principal pieces of evidence for the existence of a liquid subsurface ocean was the detection of magnetic field perturbations, in the vicinity of the satellite, that were consistent with an induced field from the interior. As Jupiter rotates, the tilted dipole causes diurnal oscillations in the magnetospheric magnetic field at the satellites, providing an alternating 'primary' or 'inducing field'. Ions dissolved in the subsurface ocean respond to this inducing field and generate eddy currents which produce a secondary or induced field that acts to exclude the varying field from

34 the conducting interior. Colburn and Reynolds (1985) first considered the consequences for electromagnetic induction
35 in the icy mantle of Europa, focusing on magnitudes of the eddy currents and their ability to heat the interior through
36 ohmic effects (see also Chyba, Hand and Thomas (2021) for a recent perspective). Kargel and Consolmagno (1996)
37 considered the induced field and concluded it could be detectable, later verified in Galileo measurements (Khurana et
38 al., 1998; Kivelson et al., 2000; Zimmer, Khurana and Kivelson, 2000; Khurana et al., 2009).

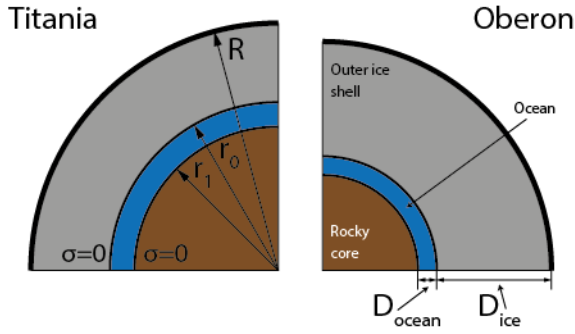
39 The strength of the induced field relative to the inducing field is a diagnostic of the extent and conductivity of the
40 subsurface ocean. Although the signature at Europa is modified by the plasma interaction of Europa's weak ionosphere
41 with Jupiter's magnetosphere, the induced field is sufficiently strong that it can be resolved against the field of the
42 plasma currents surrounding the satellite (e.g., Khurana et al., 1998; Zimmer, Khurana and Kivelson, 2000; Schilling,
43 Neubauer and Saur, 2007).

44 **1.2 Uranus' main icy satellites and their interiors**

45 In comparison to the satellites of Jupiter (and Saturn), we know very little about the main icy satellites at Uranus:
46 Miranda, Ariel, Umbriel, Titania and Oberon. These satellites show evidence of cryovolcanic resurfacing (e.g., Croft and
47 Soderblom, 1991) and tectonic activity in differing proportions; for example, Oberon is heavily cratered and less faulted
48 than Titania.

49 Hussmann, Sohl and Spohn (2006) constructed detailed models of the thermal and mechanical equilibrium of a range of
50 icy bodies in the outer solar system, including those at Uranus. They considered two- and three-layer models consisting
51 of a rocky core surrounded by two water layers and calculated the heat flux, the resulting density, pressure and
52 temperature profile, and hence an indication of whether the subsurface water layer could be in a liquid state. All
53 model solutions were constrained to satisfy the observational constraints of radius, mean density and moment of
54 inertia. Two factors that increased the likelihood of a subsurface ocean were a) a larger core size, which gives a larger
55 radiogenic heating rate and potentially higher subsurface temperature; and b) a larger fraction of NH_3 that lowers the
56 freezing point of H_2O . Their models assumed that the satellites were differentiated but this does not appear to be an
57 unrealistic assumption since the satellite surfaces are predominantly icy, yet have mean densities higher than water
58 indicating at least some differentiation of heavier material to the interior. As the authors only included radiogenic
59 heating, and not tidal heating, for example, they considered that their solutions were a lower bound on the presence of
60 subsurface oceans.

61 Among the uranian satellites, solutions with subsurface oceans were found only for Titania and Oberon. Three
62 solutions were found for Titania ($R=519.8$ km), with ocean depths of 16, 39.4 and 51.5 km and ice (I) shell thicknesses of
63 253.1, 229.7, and 217.7 km respectively. Two solutions were found for Oberon ($R=481.0$ km) with oceans between 16
64 and 39.3 km thick, overlaid by an ice (I) shell of thickness between 264.4 and 241.1 km respectively (Hussmann, Sohl
65 and Spohn, 2006). Figure 1 shows a schematic of these models.



66

67 Figure 1: Schematic of the subsurface ocean models for Titania and Oberon, based on two specific models from
 68 Hussmann, Sohl and Spohn (2006).

69

70 It is important to highlight that this does not preclude the presence of subsurface oceans at the other uranian icy
 71 satellites since the models do not predict a subsurface ocean at Enceladus, contradicting observational evidence from
 72 Cassini (e.g., Thomas et al., 2016). However, these models for Titania and Oberon provide our motivation to explore
 73 the induced response from ions dissolved in the ocean, and hence the capability of passive magnetic sounding to search
 74 for the presence of an ocean in a future mission.

75 1.3 Induction

76 Magnetic flux diffuses through the conducting regions of a satellite according to the Helmholtz equation (1) and can be
 77 derived from Faraday's law, Ampere's law, $\nabla \cdot \mathbf{B} = 0$ and Ohm's law under the assumption of spatially-uniform
 78 conductivity, sufficiently low frequencies such that displacement currents can be neglected, and an absence of
 79 advection (e.g., Khurana et al., 2009; Saur et al., 2010),

80

$$81 \quad \nabla^2 \mathbf{B} = \sigma \mu_0 \frac{\partial \mathbf{B}}{\partial t} \quad (1)$$

82

83 , where σ is the conductivity, \mathbf{B} is the magnetic field, t is time, and μ_0 is the permeability of free space. In the insulating
 84 (non-conducting) regions, e.g., an icy outer mantle, equation (1) reduces to Laplace's equation. The magnetic field can
 85 be written as a linear superposition of harmonics at frequencies ω_i , with complex amplitudes \mathbf{B}_m , plus a constant
 86 background field, \mathbf{B}_c (2).

87

$$88 \quad \mathbf{B}(t) = \mathbf{B}_c + \sum_m \mathbf{B}_m e^{-i\omega_m t} \quad (2)$$

89

90 In this work we restrict ourselves to a three-layer model consisting of an insulating core, conducting liquid water layer,
 91 and insulating mantle. Assuming that the conductivity is finite and spherically-symmetrical and the primary field

92 harmonic is spatially uniform, solution of (1) gives an expression for the secondary field as an induced dipole with a
 93 dipole moment that is a phase lagged function of the primary field,

94

$$95 \quad \mathbf{B}_{\text{sec}}(\mathbf{r}, t) = -A \exp[-i(\omega t - \phi)] \left[3(\mathbf{r} \cdot \mathbf{B}_{\text{pri}})\mathbf{r} - r^2 \mathbf{B}_{\text{pri}} \right] \frac{R^3}{2r^5} \quad (3)$$

96

97 , where \mathbf{r} is the position, t is time, \mathbf{B}_{pri} is the primary driving field at frequency ω and represents one of the harmonic
 98 terms in equation (2) ($\mathbf{B}e^{-i\omega t}$), and R is the radius of the moon. $Ae^{i\phi}$ is a complex amplitude which describes the
 99 amplitude, A , of the secondary field relative to the primary, and its phase lag, ϕ . With the simplifying assumptions
 100 above, the complex amplitude can be obtained from,

101

$$102 \quad Ae^{i\phi} = \left(\frac{r_0}{R} \right)^3 \frac{\xi J_{5/2}(r_0 k) - J_{-5/2}(r_0 k)}{\xi J_{1/2}(r_0 k) - J_{-1/2}(r_0 k)} \quad (4)$$

103

$$\xi = \frac{r_1 k J_{-5/2}(r_1 k)}{3 J_{3/2}(r_1 k) - r_1 k J_{1/2}(r_1 k)} \quad (5)$$

104

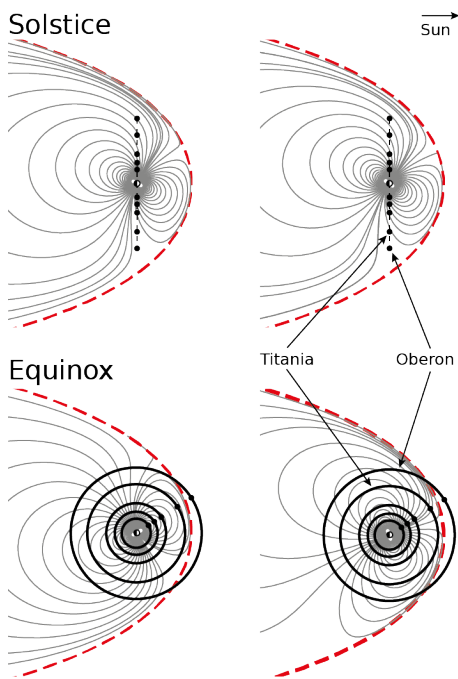
105 , where r_1 and r_0 are the radius of the inner and outer edges of the conducting layer respectively (schematically
 106 illustrated in Figure 1), k is the complex wave vector $k = (1 - i)\sqrt{\mu_0 \sigma \omega / 2}$, and J_n are Bessel functions of the first kind
 107 (e.g., Zimmer, Khurana and Kivelson, 2000).

108 **1.4 The uranian magnetosphere: factors affecting the primary field**

109 There are three key differences between the magnetospheres of Jupiter and Uranus that we must consider in
 110 understanding the primary field at the satellites, and which guide us in how we may need to treat these systems
 111 differently. Figure 2 shows a schematic of Uranus' planetary system at two different seasons and two different rotation
 112 phases (separated by half a planetary rotation, ~ 8.5 hours).

- 113 1. Large dipole tilt: Uranus' dipole axis is tilted by an angle of 60° relative to its rotation axis, and furthermore
 114 has an offset that may be important for the closer satellites such as Miranda, and possibly Ariel.
- 115 2. Proximity of the magnetopause: Even Callisto, the most distant Galilean satellite, is only around half the
 116 distance from Jupiter to the magnetopause, whereas Titania and Oberon have semi-major axes of $17.1 R_U$ and
 117 $22.8 R_U$ respectively compared with the subsolar magnetopause distance of around $19 R_U$ (see section 2.1),
 118 where $1 R_U = 25\,559$ km. Hence, Oberon is likely to orbit outside the magnetopause at certain orbital
 119 phases, seasons and solar wind conditions, with Titania less likely to spend time outside the magnetosphere.
- 120 3. Large obliquity: Uranus' $\sim 97^\circ$ obliquity implies strong seasonal behaviour that we must consider. For
 121 example, near solstice the satellite orbital planes lie close to the terminator plane, whereas near equinox they
 122 are approximately in the noon-midnight plane of the magnetosphere. At solstice Oberon rarely leaves the

123 magnetosphere whereas at equinox it periodically enters the magnetosheath. This implies that we must
124 consider the primary field at different seasons.



125

126 Figure 2: Schematic of Uranus' magnetosphere and planetary system for two rotational phases separated by half a
127 planet rotation (left, and right columns), and two seasons (top and bottom). The satellites are represented by black
128 filled circles, the satellite orbits/orbital plane by black circles (equinox) and black dashed line (solstice). Field lines are in
129 grey and the magnetopause is the red bold dashed line. Only the orbits for Titania and Oberon are indicated for clarity.

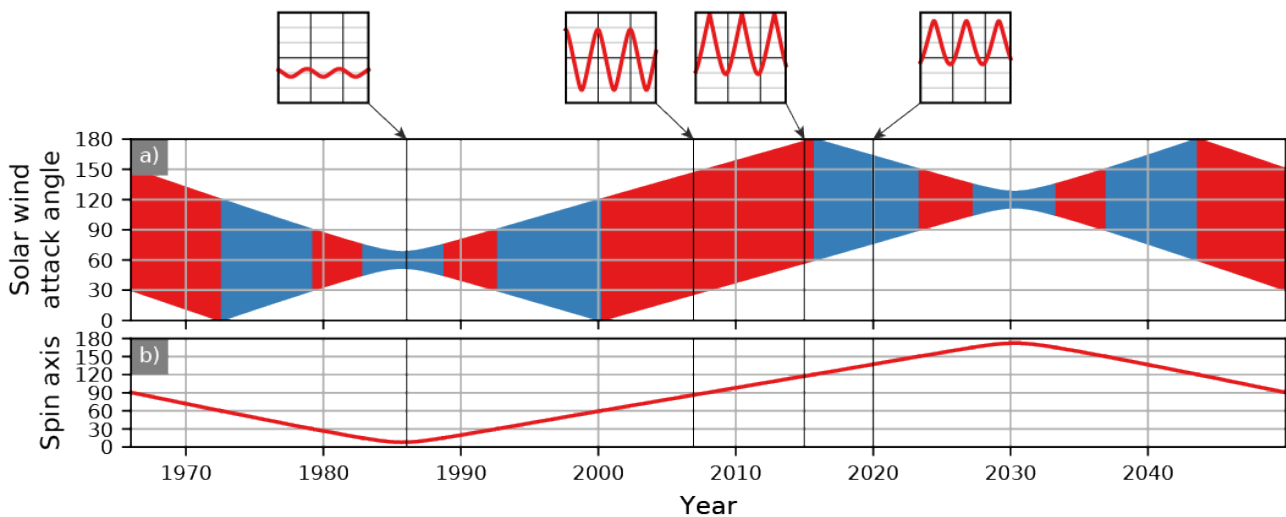
130

131 The configuration of the magnetosphere at a given moment can be coarsely parameterised by the solar wind attack
132 angle (e.g., Lepping, 1994) which is the angle, α , that the dipole axis makes to the solar wind (where $\alpha=0$ represents the
133 dipole pointing into the solar wind). Earth's magnetosphere has an attack angle of $\approx 90^\circ \pm 30^\circ$ which means that the
134 dipole is more-or-less perpendicular to the incoming solar wind flow and varies only slightly with Earth's rotation. The
135 combination of large dipole tilt and obliquity at Uranus means that near solstice the attack angle is relatively constant
136 (the magnetosphere essentially rotates around the planet-Sun line) but at equinox the dipole can, at times, be pole-on
137 to the solar wind (Figure 2 bottom right) and so the solar wind attack angle can vary considerably over one Uranus
138 rotation. These significant diurnal and seasonal variabilities are a unique feature of the uranian magnetosphere (e.g.,
139 Lepping, 1994; Arridge and Paty, in press).

140 Figure 3 shows the solar wind attack angle for one Uranus year (approximately 84 years). The variation can be thought
141 of a slowly varying mean solar wind attack angle representing seasonal variations with a high frequency diurnal
142 variation forming an 'envelope' around the mean. The figure also shows the angle between the spin axis and the solar
143 wind that informs us about the orientation of the satellite orbital plane relative to the Sun (e.g., the changing
144 orientation in Figure 2). These two angles expose the different characteristics of the dipole-solar wind geometry and
145 satellite orbital plane-solar wind geometry over time. We split this time series into 'zones' to reflect different

146 characteristics at different epochs. The solar wind attack angle is quantised into 45° segments, for example where $0 \leq$
 147 $\alpha < 22.5^\circ$ would be represented by 0°, $22.5^\circ \leq \alpha < 67.5^\circ$ by 45°, and $67.5^\circ \leq \alpha < 112.5^\circ$ by 90°. Thus we coarsely
 148 represent the attack angle as quasi-pole-on, intermediate, and quasi-perpendicular, etc.. The spin axis angle is similarly
 149 quantised into 30° segments. Each unique combination of quantised attack angle and spin axis angle forms a unique
 150 ‘zone’ that represents some quantised representation of the geometry of Uranus’ magnetosphere and its seasonal and
 151 diurnal variation.

152 For example, near the Voyager 2 flyby in 1986, the solar wind attack angle was quasi-perpendicular to the solar wind
 153 and the spin axis was approximately parallel to the solar wind implying that the satellites only experienced the
 154 magnetospheric flanks and polar regions over an orbit, never encountering the dayside and nightside. Whereas during
 155 2015, the magnetosphere transitioned between pole-on and perpendicular configurations over a diurnal rotation and
 156 the spin axis was perpendicular to the solar wind implying that the satellites experienced the nightside and dayside of
 157 the magnetosphere every orbit.



158
 159 Figure 3: Angles between (a) the solar wind and dipole (attack angle) and (b) the solar wind and spin axis for a full
 160 Uranus orbit. Insets show diurnal variation of the solar wind attack angle at different epochs. Non-sinusoidal
 161 behaviour in the solar wind attack angle is particularly evident near 2015. Banding indicates the division of the time
 162 series into particular ‘zones’ that have similar characteristics. There is no specific meaning to the colouration.

163
 164 Apart from being a useful intuitive tool, the variations in the solar wind attack angle have implications for the primary
 165 field at the satellites. The distribution and magnitude of currents on the magnetopause change with solar wind attack
 166 angles and so affect the primary field by changing the contribution from the magnetopause currents. Furthermore, as
 167 can be seen in the insets, the solar wind attack angle variation is also not purely sinusoidal so introduces additional
 168 harmonics to the diurnal variation of the magnetopause field. Although the solar wind attack angle is a useful and
 169 intuitive tool, the real configuration can be quite difficult to fathom as the field is truly three-dimensional and simple 2D
 170 cuts do not fully capture the configuration (Arridge and Paty, in press); 3D tools are essential in understanding the
 171 geometry at a given epoch (Arridge and Wiggs, 2019).

172 1.5 Motivation

173 In this paper we explore the induced response from sub-surface oceans that have been suggested to exist within Titania
174 and Oberon. Hence, we explore the capability of passive magnetic sounding to provide empirical evidence for the
175 presence of an ocean, as carried out at Europa (Khurana et al., 2009), and examine whether such oceans might be
176 detectable by potential future missions. Furthermore, because Uranus' magnetosphere is so diurnally-variable, and this
177 variability changes with season, there may be seasons where an induced response from the oceans is richer and which
178 might provide additional opportunities to learn more about these elusive worlds through multi-frequency passive
179 sounding. Although we focus primarily on Titania, we have learned from the Cassini mission that small icy bodies can be
180 more active than previously thought and so we also include some examination of the inducing field at Uranus' other
181 satellites. We first construct a model for the magnetospheric magnetic field at Uranus and use it to calculate the
182 primary field at each of Uranus' main satellites over a Uranus orbit (section 2). The amplitude of the primary field
183 harmonics are evaluated in section 3 and applied to compute the induced response using the internal structure models
184 of Hussmann, Sohl and Spohn (2006). Finally, we estimate the field at Titania during potential satellite flybys and
185 conclude that the calculated subsurface oceans from Hussmann, Sohl and Spohn (2006) would result in a detectable
186 induced signature from a flyby of this satellite.

187 2. Methods

188 2.1 Magnetospheric magnetic field model

189 To calculate the primary (inducing) field at the satellites we require a model for the magnetospheric magnetic field. In
190 the terrestrial magnetosphere, the principal contributions to this field are the internal (planetary) magnetic field, the
191 field of the Chapman-Ferraro (magnetopause) currents, the field of the ring current, and the field of the cross-tail
192 current sheet (e.g., Tsyganenko, 2002). At Jupiter and Saturn these must also be augmented by the field of a
193 magnetodisc current sheet which has a dramatic effect on the near-equatorial field (e.g., Smith et al., 1974; Arridge and
194 Martin, 2018). At Uranus we only include the internal planetary field and the Chapman-Ferraro field. Voyager 2
195 observations demonstrated the presence of a well-developed helical tail current sheet at solstice (Behannon et al.,
196 1987), however, its geometry for other solar wind attack angles, e.g., at equinox with periods in both pole-on and
197 perpendicular orientations, is much more complex and so we chose not to include a tail current sheet. The implications
198 of this will be considered shortly. In contrast to the tail current sheet, Voyager 2 observations suggested a very weak
199 ring current, relative to the internal field, around an order of magnitude smaller than that at Earth (Connerney et al.,
200 1987) and so we chose not to include this in our model. We use the most recent internal field model, which uses
201 magnetometer data and ultraviolet auroral data from Voyager 2 to constrain a 4th degree (hexapole) spherical
202 harmonic model 'AH₅' (Herbert, 2009).

203 The final ingredient is a geometrical model for the magnetopause. We use the functional form introduced by Shue et
204 al. (1997) where a position (r, θ) on the magnetopause (with θ measured from the planet-Sun line) is given by $r =$
205 $r_0 [2(1 + \cos \theta)^{-1}]^\xi$ where r_0 is a constant representing the distance to the subsolar point on the magnetopause and ξ
206 is a constant that describes the shape of the magnetopause, with $\xi > \frac{1}{2}$ representing a magnetopause that flares out

207 with distance downtail. These constants were derived by approximately matching the shape of the magnetopause in
 208 the MHD simulations of Tóth et al. (2004, their Figure 5) yielding constants $r_0 = 19 R_U$ and $\xi = 0.72$. This geometry
 209 was fixed for all of our calculations and was not varied with solar wind dynamic pressure (discussed further below), or
 210 varied to reflect different seasonal/diurnal configurations. This would be expected to introduce additional variations in
 211 the magnetic field at the appropriate periods, but since we have little information to calculate such changing geometry
 212 we chose to exclude such effects.

213 The effect of the Chapman-Ferraro currents is to ‘confine’ or ‘shield’ the magnetic field inside the magnetopause such
 214 that no magnetic flux crosses the boundary. This corresponds to a condition where the magnetic field normal to the
 215 magnetopause is zero everywhere on the boundary. In our model we only consider the field of the planet, \mathbf{B}_{int} , and so
 216 we can state this problem as a zero-valued integral over the boundary. For the practical purpose of finding a Chapman-
 217 Ferraro field, \mathbf{B}_{mp} (and its parameters, $\boldsymbol{\theta}$), that confines the planetary field within the magnetopause, it is sufficient to
 218 consider the minimisation of a sum over a finite number, N , of points, \mathbf{r}_i , on the magnetopause with unit normal
 219 vectors $\hat{\mathbf{n}}(\mathbf{r}_i)$ (Schulz and McNab, 1996):

220

$$221 \quad \min \left[\frac{\sum_{i=0}^{N-1} [(\mathbf{B}_{int}(\mathbf{r}_i) + \mathbf{B}_{mp}(\mathbf{r}_i, \boldsymbol{\theta})) \cdot \hat{\mathbf{n}}(\mathbf{r}_i)]^2}{N} \right]^{\frac{1}{2}} \quad (6)$$

222

223 As the Chapman-Ferraro currents flow entirely on the surface of the magnetopause, their field is curl-free inside the
 224 magnetosphere and can be represented by the gradient of a scalar magnetic potential, $\mathbf{B}_{mp} = -\nabla U$, and so U can be
 225 solved from Laplace’s equation using suitable eigenfunctions as appropriate for the geometry of the magnetopause.
 226 We used a modified form of Cartesian ‘box’ harmonics (Tsyganenko, 2002, equations 30-32) with separate harmonics to
 227 confine the part of the internal field parallel, $U_{||}$, and perpendicular, U_{\perp} , to the planet-Sun line: $\mathbf{B}_{mp} = -\nabla U_{\perp} - \nabla U_{||}$:

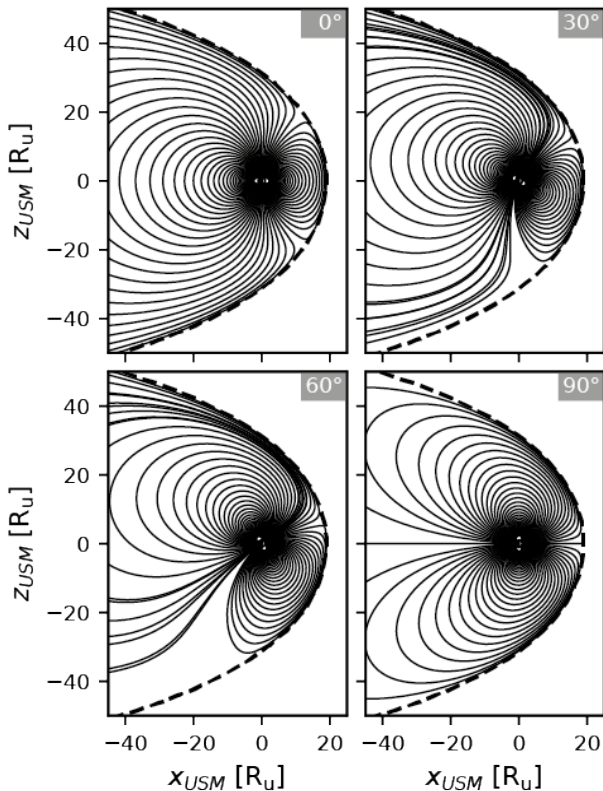
$$228 \quad U_{||}(x, y, z) = \sum_{j=1}^4 \sum_{l=1}^4 (c_{jl} \sin \Psi + d_{jl} \sin 2\Psi) \exp \left[x \sqrt{\frac{1}{q_j^2} + \frac{1}{s_l^2}} \right] \cos \frac{y}{q_j} \cos \frac{z}{s_l} \quad (7)$$

$$229 \quad U_{\perp}(x, y, z) = \sum_{i=1}^3 \sum_{k=1}^3 (a_{ik} \cos \Psi + b_{ik} \cos 2\Psi) \exp \left[x \sqrt{\frac{1}{p_i^2} + \frac{1}{r_k^2}} \right] \cos \frac{y}{p_i} \sin \frac{z}{r_k} \quad (8)$$

230 where a , b , c and d are amplitude coefficients, q , s , p and r are scale parameters, $\Psi = \frac{\pi}{2} - \alpha$ is the dipole tilt angle,
 231 and x , y , and z are coordinates in the right-handed Uranocentric Solar Magnetospheric (USM) system, where $\hat{\mathbf{e}}_x$ is the
 232 unit vector from Uranus to the Sun, and the X-Z plane contains the dipole vector, \mathbf{M} , such that $\hat{\mathbf{e}}_y = \hat{\mathbf{M}} \times \hat{\mathbf{e}}_x$. Equations
 233 (7,8) include 25 harmonics with 64 free parameters to be found through the minimisation of (6).

234 As the quadrupole and higher degree terms are weak at the magnetopause, only the dipole component was included in
 235 the minimisation of (6) with a dipole moment of 23000 nT (Connerney et al., 1987). For simplicity the dipole offset was
 236 not included in this computation, but only causes a scalar error of less than $\delta B = 3B \frac{dr}{r} \sim 0.06$ nT in the field strength
 237 at the magnetopause, smaller than the quadrupole field at the magnetopause. The minimisation was performed using

238 the Downhill Simplex algorithm (Nelder and Mead, 1965) as implemented in the Python package SciPy (Virtanen et al.,
 239 in press). The minimiser was iteratively called, each time increasing the number of points that the field was evaluated
 240 on, until the root-mean-square normal field and maximum absolute normal field were less than 0.005 nT and 0.01 nT
 241 respectively, or until the optimiser had terminated successfully four times in a row. The optimisation of (6) was
 242 completed with 37440 points with a root-mean-square normal field of 0.00199 nT and a maximum normal field of
 243 0.0104 nT. Figure 4 shows field lines traced for four different dipole tilt angles showing the quality of the
 244 magnetopause shielding and the coefficients required for equations (7) and (8) are included in the appendix.



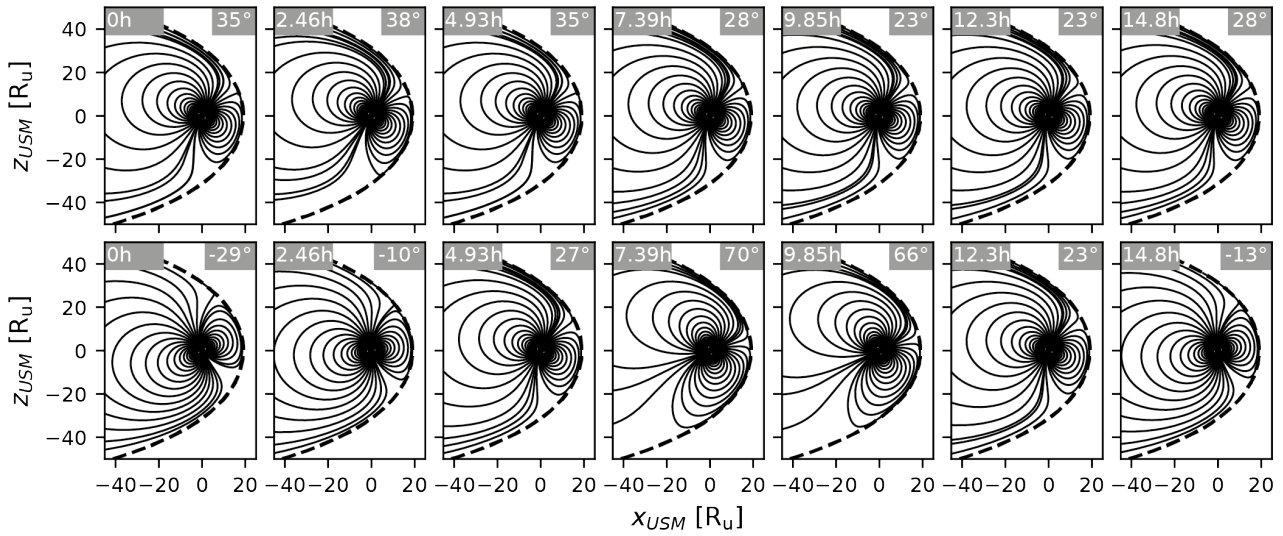
245

246 Figure 4: Shielded dipole field lines for dipole tilt angles of 0, 30, 60, and 90 degrees in the USM X-Z plane. Field lines
 247 are drawn from seed points on a circular slice of the planet at 2 degree intervals.

248

249 The entire model was built in Python using NumPy (Oliphant, 2006), SciPy and the SPICE toolkit (Acton, 1996) via
 250 SpiceyPy (Annex et al., 2020) packages, and a custom magnetic field modelling package. As the AH₅ model is defined in
 251 the Uranus Longitude System (ULS) (Connerney et al., 1986) (also known as the U1 coordinate system) which has its
 252 pole opposite to that of the IAU defined pole of Uranus, the model was constructed in these coordinates with
 253 conversions to/from USM as necessary. USM coordinates can become degenerate for the case where the dipole is
 254 exactly parallel or anti-parallel to the solar wind, where the orientation of the X-Z plane around the X axis becomes
 255 undefined. This was not encountered during the period of study. Figure 5 shows the diurnal structure in the field for
 256 the Voyager 2 epoch, where the configuration remained largely static with the field rotating around the planet-Sun line,
 257 and January 2000 where considerable changes in configuration are found over a diurnal cycle. Figure 6 shows a

258 comparison of the residual field, with the AH_5 internal field model subtracted, and the model at the Voyager 2 flyby.
259 The model comparison is generally very good on the dayside, with a significant discrepancy near closest approach
260 (possibly reflecting additional unconstrained structure in the internal field) but is worse on the nightside where our
261 neglect of the tail field can be seen.

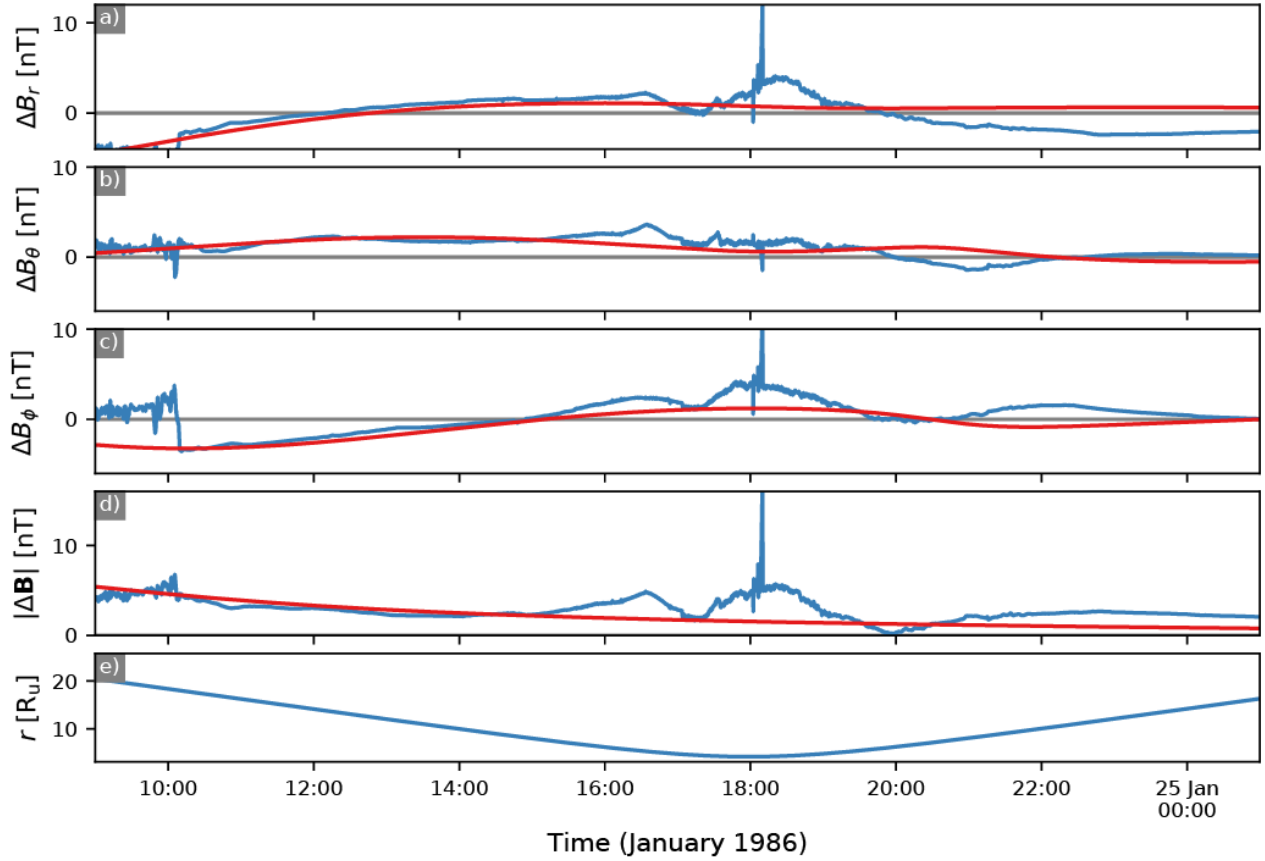


262

263 Figure 5: Field lines traced every $1/7^{\text{th}}$ of a planetary rotation for the Voyager 2 epoch (top) and January 2000 (bottom).

264 Each panel contains the dipole tilt angle at that time.

265



266

267 Figure 6: Comparison of the external field model (dipole shielding, red) and residual field in blue in spherical polar
 268 coordinates in the U1 coordinate system. The radial distance of Voyager 2 from Uranus is plotted in panel (e).

269

270 The model has the capability to be varied with the upstream solar wind dynamic pressure through changes in the size of
 271 the magnetosphere. We do not include this effect for two reasons: a) to focus on the seasonal and geometrical effects,
 272 and b) due to the difficulty in constructing a physically-meaningful timeseries of solar wind pressure over a period of 84
 273 years, from a short time series around the Voyager 2 mission. We leave this for future work. However, experiments
 274 show that for near solstice conditions using Voyager 2 data the amplitude of such variations amount to ~ 0.1 nT at both
 275 Titania and Oberon. As might be expected, there are also harmonics of the solar rotation period ~ 500 hours and
 276 frequency mixing with orbital periods that amount to a ~ 0.01 nT amplitude.

277 2.2 Construction of the time series data set

278 As we were particularly interested in the seasonal effects within the system and were concerned to include effects such
 279 as nodal precession (e.g., Jacobson, 2014a), we used SPICE to compute the positions of the satellites, rather than using
 280 mean orbital elements as in other studies in the jovian system analyses (e.g., Seufert, Saur and Neubauer, 2011). The
 281 positions of Miranda, Ariel, Umbriel, Titania and Oberon were calculated between 01 January 1966 and 01 July 2050,
 282 bounding a full Uranus year. The time series was constructed at a cadence of 300 s which produces around 400 data
 283 points during one orbit of Miranda and approximately 2500 for Titania. The magnetic field model was used to compute

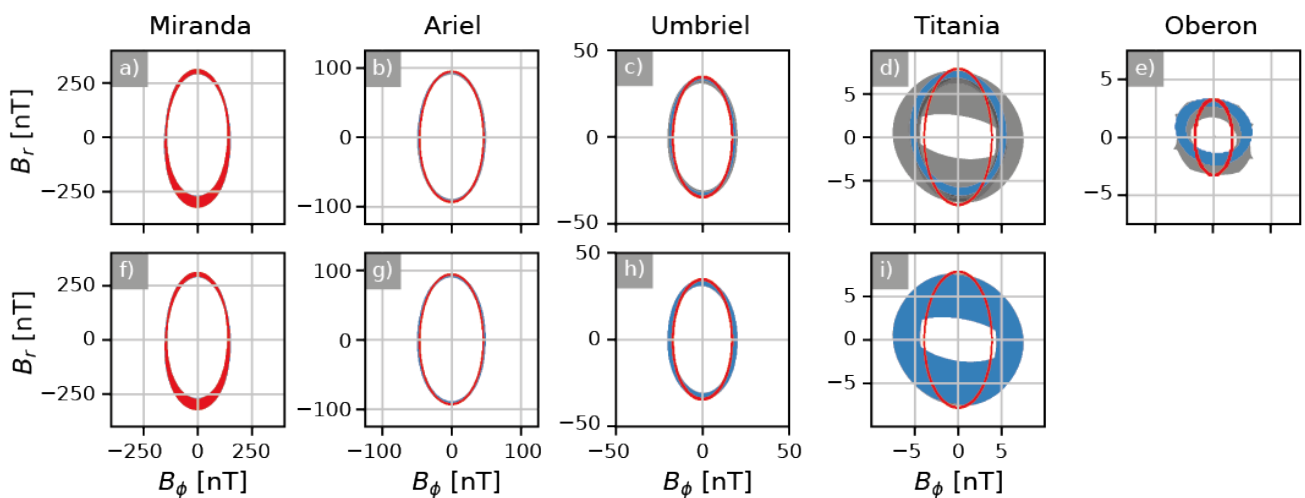
284 the field at each satellite and the individual sources (dipole, quadrupole, octapole, hexapole, magnetopause) were
 285 saved along with the total. Data was stored in HDF5 files for further analysis and are publicly available at
 286 doi:10.17635/lancaster/researchdata/411. During analysis a discrepancy was noted between the orbital period of the
 287 satellites (from mean elements) and the data from SPICE and so we also computed the orbital period from SPICE for
 288 consistency with the analysis. Orbital elements were obtained from state vectors using SPICE using a GM of
 289 $5.793951322279009 \times 10^6 \text{ km}^3 \text{ s}^{-2}$ from ephemeris URA112 (Jacobson, 2014b).

290 3. Analysis of the inducing field

291 3.1 General overview

292 Figure 7 shows hodograms of the magnetic field in the $B_\phi - B_r$ plane for the five satellites near solstice and near
 293 equinox. In this plane the hodograms have an elliptical polarisation however in the $B_\theta - B_r$ plane they are almost
 294 linearly polarised, in common with similar analyses in the jovian system (Seufert, Saur and Neubauer, 2011). The finite
 295 thickness in B_r extrema for Miranda is due to the eccentricity of Miranda's orbit. As expected, the hodograms show
 296 increasing departures from the dipole model (indicated in red) with increasing orbital distance, and increasing
 297 differences between seasons, just visible at Umbriel to significant at Titania. Interestingly, the hodogram is relatively
 298 constrained near solstice, possibly due to the narrow range of solar wind attack angles at that time and that the orbits
 299 are almost in the terminator plane. We do not show the hodogram for Oberon at equinox due to the regular
 300 excursions outside the magnetosphere when the satellite is on the dayside. In the jovian system between Ganymede
 301 and Callisto, the field becomes almost linearly polarised which is a consequence of the magnetodisc current sheet
 302 (Seufert, Saur and Neubauer, 2011). This is absent at in our model results, partly due to the lack of such a current sheet
 303 at Uranus, but also due to our neglect of a tail current sheet which would introduce some linear polarisation at
 304 particular orbital phases. This may affect Titania but would most strongly affect Oberon.

305



306

307 Figure 7: Hodograms for the variation of the field in the $B_\phi - B_r$ space for the five satellites in two epochs (near solstice
 308 (a-e) and near equinox (f-i). The near equinox hodogram for Oberon is not shown due to periods spent outside of the

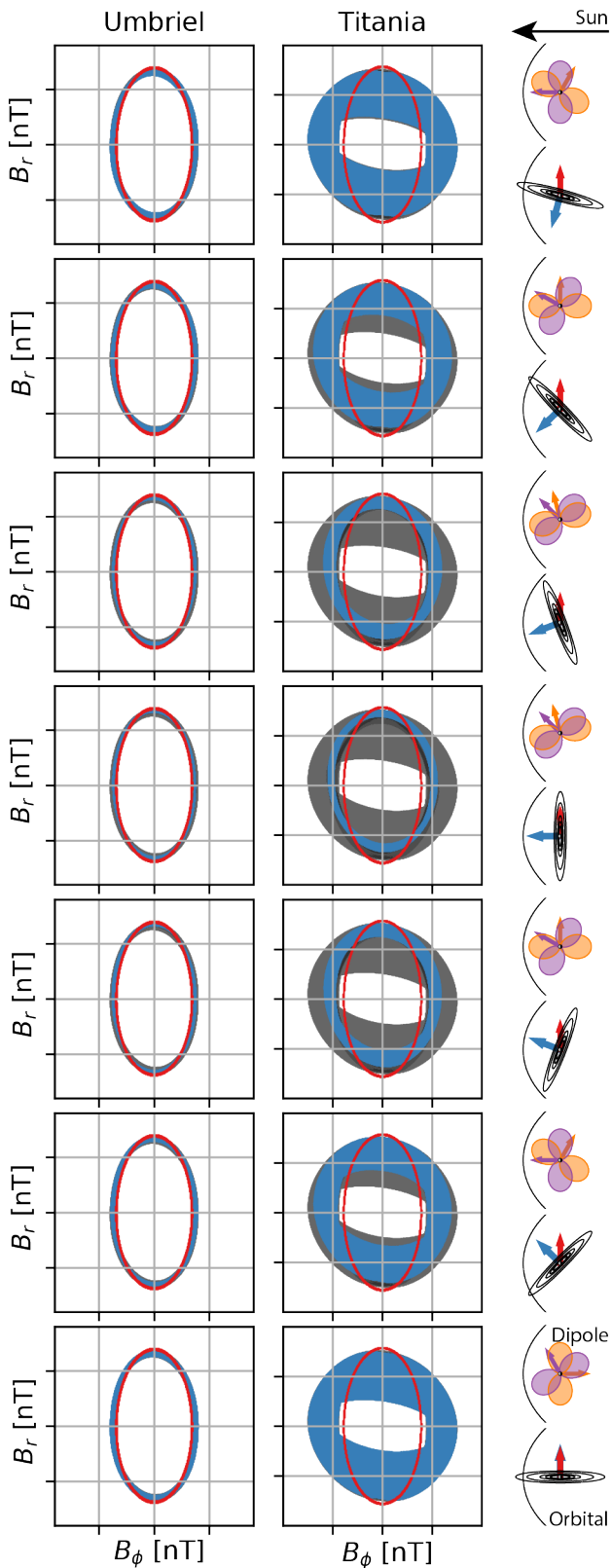
309 magnetosphere. Grey backgrounds indicate the envelope of the whole hodogram over an entire Uranus orbit covering
310 the most highly-visited part of the hodogram space; the red envelope is just the hodogram from the dipole component
311 of Uranus' field at the satellite; and the blue envelope shows the total field.

312

313 To explore the seasonal variation in more detail, Figure 8 shows hodograms for Umbriel and Titania over half a Uranus
314 orbit. As expected due to its smaller orbital distance, the hodograms for Umbriel display relatively little variation
315 compared to Titania, however, the hodograms for Umbriel are more elliptically-polarised near solstice, and more
316 circular near equinox. The hodograms for Titania show a large degree of variation with season. Near solstice, in the
317 centre two rows of Figure 8, the hodogram has a relatively narrow elliptical polarisation and occupies a relatively small
318 fraction of the overall envelope of variation over a Uranus year. Near equinox it is broader and almost circular, but it
319 must be highlighted that these intervals are over a wider period of time which may also contribute to the breadth of
320 the hodogram. These changes in the hodograms around equinox are not completely correlated with changes in the
321 range of solar wind attack angles, but more associated with the changing orientation of the equatorial plane relative to
322 the Sun. Near solstice, the equatorial plane is almost perpendicular to the planet-Sun line and so the satellite orbits
323 roughly in the terminator plane, whereas near equinox the planet-Sun line is roughly in the plane of the equator and
324 the orbits take satellites between the dayside and nightside every orbit. Seasonal variations in the inducing (primary)
325 field should also produce seasonal variations in the amplitude of different driving periods, and hence seasonal
326 variations in the induced (secondary) field. This has clear consequences for the exploration of the icy satellites at
327 different epochs; particular epochs may present a richer scenario for the detection and study of subsurface oceans.

328

329



330

331 Figure 8: Hodograms for Umbriel (left) and Titania (right) for different seasons. The sketches on the right show the
 332 configuration of the system; at the top of each panel field lines at a fixed L-shell show extrema (orange and purple) of
 333 the diurnal motion of the dipole with respect to the Sun, and the bottom of each panel shows the orientation of the
 334 satellite system, spin axis in blue, with the orbital velocity vector in red. Both sketches have the Sun off to the left-hand

335 side, the top panel is projected into the plane of the dipole magnetic field and the planet-Sun line, the bottom panel is
336 viewed from above the orbital plane. The curved surface represents the magnetopause. For clarity, the axis scales
337 have been suppressed but they have the same ranges and grid as those in Figure 7. Representative centre-times for
338 each row are approximately 1970, 1976, 1982, 1986, 1991, 1996.

339

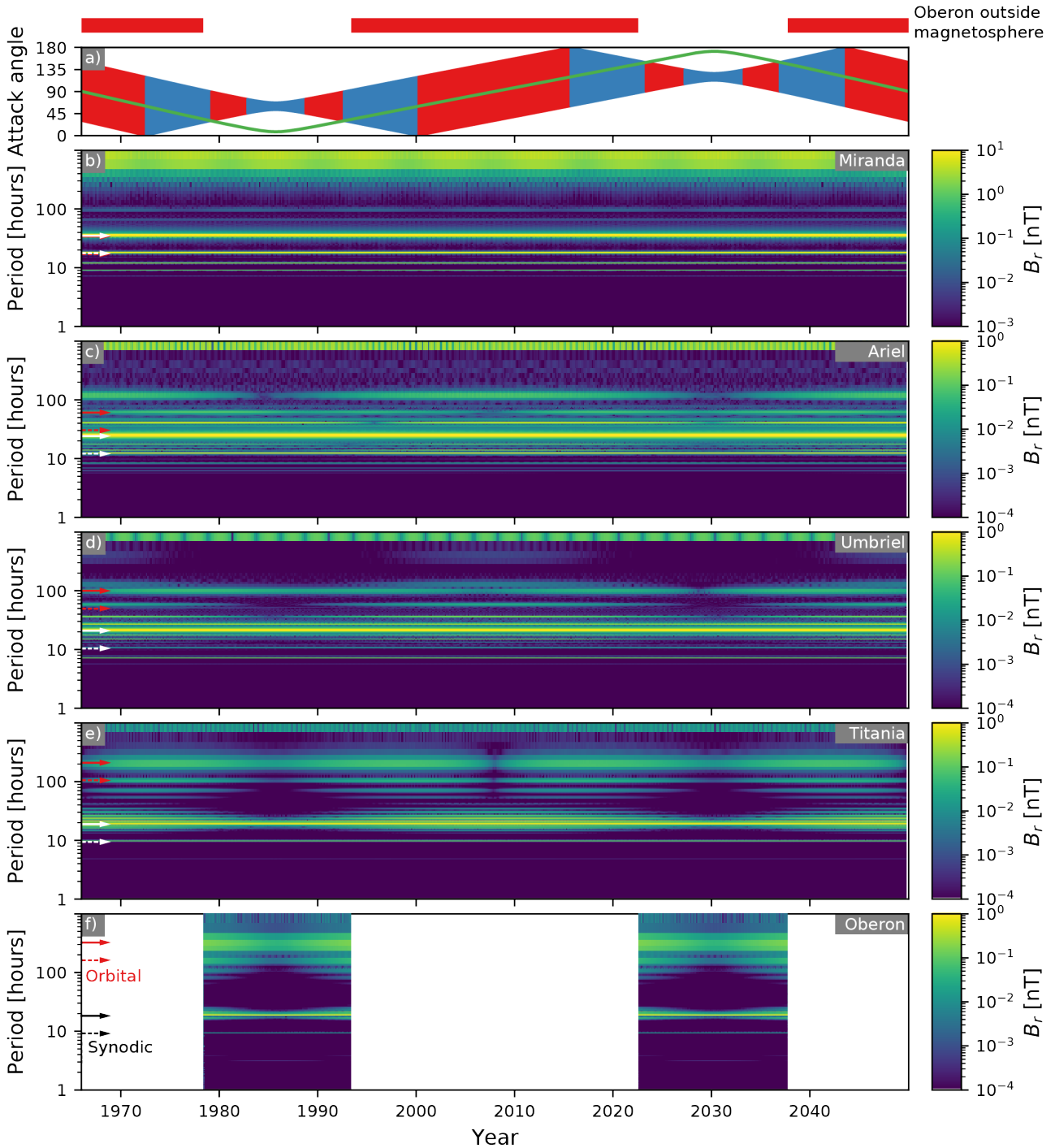
340 **3.2 Spectral analysis overview**

341 From these time series we estimated the power spectral density using `scipy.signal` both in the form of line
342 spectra (Welch, 1967) and spectrograms. In both cases a Hamming window was used and was chosen to provide a
343 balance between with the width of main lobe and relative amplitude of the side lobes. The number of samples used for
344 spectral estimation was determined algorithmically to give good resolution near relevant periods. Specifically we
345 required $\Delta t/T$ of 5% at 17 hours (approximate rotation period of Uranus) and 10% at 200 hours (approximate orbital
346 period of Titania) with the constraint that the number of samples was a power of two. This required $2^{16}=65536$
347 samples and $\Delta t/T$ of 0.311% and 3.662% for 17 and 200 hours respectively. The maximum period that could be
348 examined was 5461 hours (4 s.f.). Time series were linearly detrended before spectral estimation, although the effects
349 of detrending on the power spectral density were examined and did not find any significant differences between the
350 choices of detrending (constant Vs. linear). Spectrograms were not calculated with overlaps between samples but line
351 spectra used the `scipy.signal.welch` default of half the number of samples per windowed interval (32768 in this
352 case).

353 Figure 9 shows spectrograms of the B_r component of the total magnetic field for each main icy satellite as a function of
354 time. As noted earlier, and schematically illustrated in Figure 2, Oberon has an orbit that takes it outside the
355 magnetosphere, indicated in Figure 9 by bars at the top of the figure. Such excursions are not found near solstice when
356 the spin axis is approximately parallel to the solar wind, and where the satellite orbits are in a plane perpendicular to
357 the solar wind. In our synthetic time series these excursions outside the magnetosphere give a null field (by
358 construction). Hence, we exclude these intervals from the spectral analysis. In each panel we indicate the orbital and
359 synodic period, the beat period between the orbital and Uranus rotation period, $T_{\text{syn}} = \left[\frac{1}{T_{\text{ura}}} - \frac{1}{T_{\text{orb}}} \right]^{-1}$, and their
360 second harmonics.

361 At each satellite the amplitude at the synodic period is approximately constant in time, however, the amplitude at the
362 orbital period exhibits variation over an order of magnitude between different epochs. Near solstice, where the angle
363 between the solar wind and the spin axis is near 0° or 180° , the time series shows relatively low amplitudes at the
364 orbital period and its harmonics and the spectrum is relatively simple and uncluttered. Near equinox, where the angle
365 between the solar wind and the spin axis is approximately 90 degrees, there is significant power at the orbital period
366 and its harmonics and also a plethora of other spectral peaks, particularly at periods not consistent with either periods
367 or their harmonics. These additional spectral peaks are more important for Titania, less important for Umbriel and
368 Ariel, and essentially absent (relative to the main peaks) at Miranda. As expected, the dipole field component appears
369 at the synodic period, and occasionally at the orbital period if there are effects due to orbital eccentricity of the

370 satellite. The quadrupole field appears at the synodic period in B_θ and the 2nd harmonic in B_r and B_ϕ due to the
 371 symmetry of the quadrupole. The magnetopause field always appears at the orbital period of the satellites due to the
 372 changing position of the satellite relative to the magnetopause over an orbit. There is also power from the
 373 magnetopause field at the synodic period of the satellites due to the variation in dipole tilt over a planetary rotation.



374

375 Figure 9: Amplitude spectra for the radial component of the magnetic field at each of the main icy satellites as a
 376 function of time. Intervals where Oberon spends periods is outside the magnetosphere (indicated by the red bars at
 377 the top of the figure) have not been analysed leaving blank spaces in panel (f). The orbital and synodic periods are

378 indicated by red and black/white arrows respectively, with the fundamental frequency as a solid line and the higher
379 harmonics as dashed lines. Panel (a) also shows a summary of the solar wind attack angle and spin axis-solar wind
380 angle from Figure 3.

381 The fine spectral structure we see in Figure 9 was determined to be due a set of heterodynes, caused by mixing of
382 different frequency components: $T_{het\pm} = \frac{1}{T_1} \pm \frac{1}{T_2}$. This was found to be a persistent feature in the magnetopause field
383 due to a mixing of the synodic period with the orbital period and its harmonics, interpreted as the motion of the
384 satellite through an asymmetrical magnetopause cavity thus experiencing a magnetopause field that varies over an
385 orbit. Weaker heterodynes, from mixing of the orbital period with higher harmonics of the synodic period, are
386 interpreted as a consequence of the non-sinusoidal behaviour of the solar wind attack angle over a rotation period. For
387 example, at solstice Titania experiences relatively symmetrical motion relative to the magnetopause as the orbit is
388 roughly in the terminator plane and so the satellite remains near the flanks of the magnetopause. Near equinox,
389 Titania experiences both the dayside and nightside magnetosphere and so experiences an asymmetrical magnetopause
390 field over an orbit. As expected, the heterodyne spectrum is much richer near equinox. There are some hints of such
391 behaviour in similar power spectra for Ganymede presented by Seufert et al. (2011), although the resolution of their
392 spectra is much lower and the amplitudes are smaller, as expected for satellites that are much farther from the
393 magnetopause.

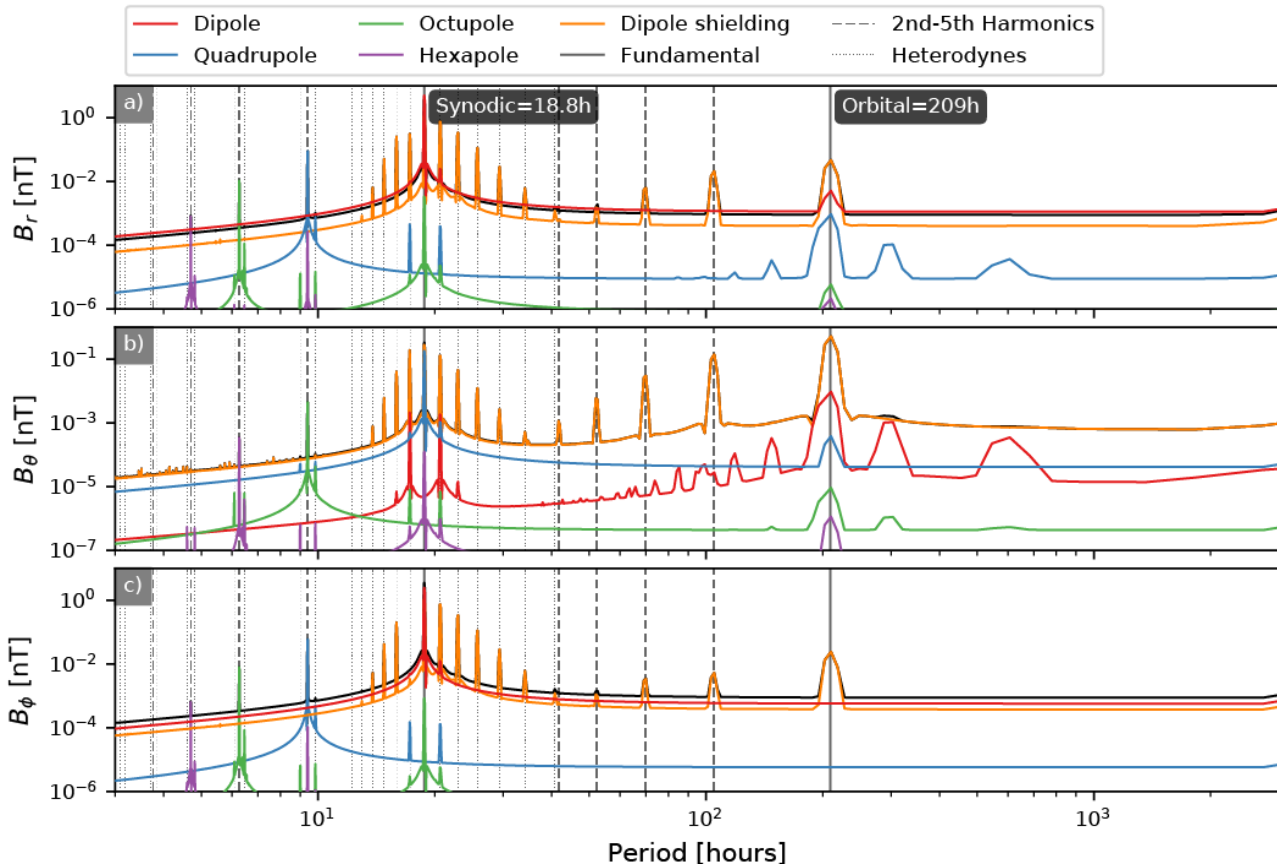
394 **3.3 Line spectra: Titania and Miranda**

395 Figure 10 shows the amplitude spectrum for each field component at Titania near equinox. This spectrum is similar to
396 that near solstice but with larger amplitude heterodynes at equinox. The solstice spectrum for Titania is also similar to
397 Oberon near solstice. The plot highlights the fundamental periods, their harmonics, and heterodynes. Generally the
398 fundamental period and the second harmonics are the strongest lines. For clarity we do not plot heterodynes amongst
399 higher harmonics of both the orbital and synodic periods but note that heterodynes between harmonics generally have
400 a much lower amplitude. As expected for the orientation of the internal field, B_r and B_ϕ have the larger amplitudes
401 amongst the internal field terms. The magnetopause field is somewhat different since the orientation of our spherical
402 coordinate system with respect to the solar wind direction strongly varies with season due to the large obliquity. The
403 magnetopause field presents a great deal of fine structure in the form of heterodynes near the synodic period.

404 Some additional structure associated with the internal field can be seen near the orbital period, for example signals at
405 around 300 and 600 hours, and are not predicted by sets of heterodynes between the orbital and synodic periods.
406 With the assumption that these are additional heterodynes, they require a modulating signal with a period of around
407 600 hours to produce heterodynes between the orbital period and the fundamental and 2nd harmonic of this
408 modulating period. Without an obvious source within the system, and its restriction to the internal field, made us
409 suspect this was perturbations in the satellite orbits. We computed power spectra of the orbital elements and found a
410 range of spectral peaks in the semi-major axis (computed using SPICE) of Titania matching the periods of low-amplitude
411 peaks in our field data. Similar spectral peaks were also found in the orbit of Oberon and which match similar spectral
412 peaks in the spectrum of Oberon. This also provides an interpretation for the signals near 1000 hours seen in Figure 9.

413 This was sufficient for us to conclude a non-magnetospheric effect and conclude that this was to do with the orbital
 414 evolution of the satellites and we made no further investigation.

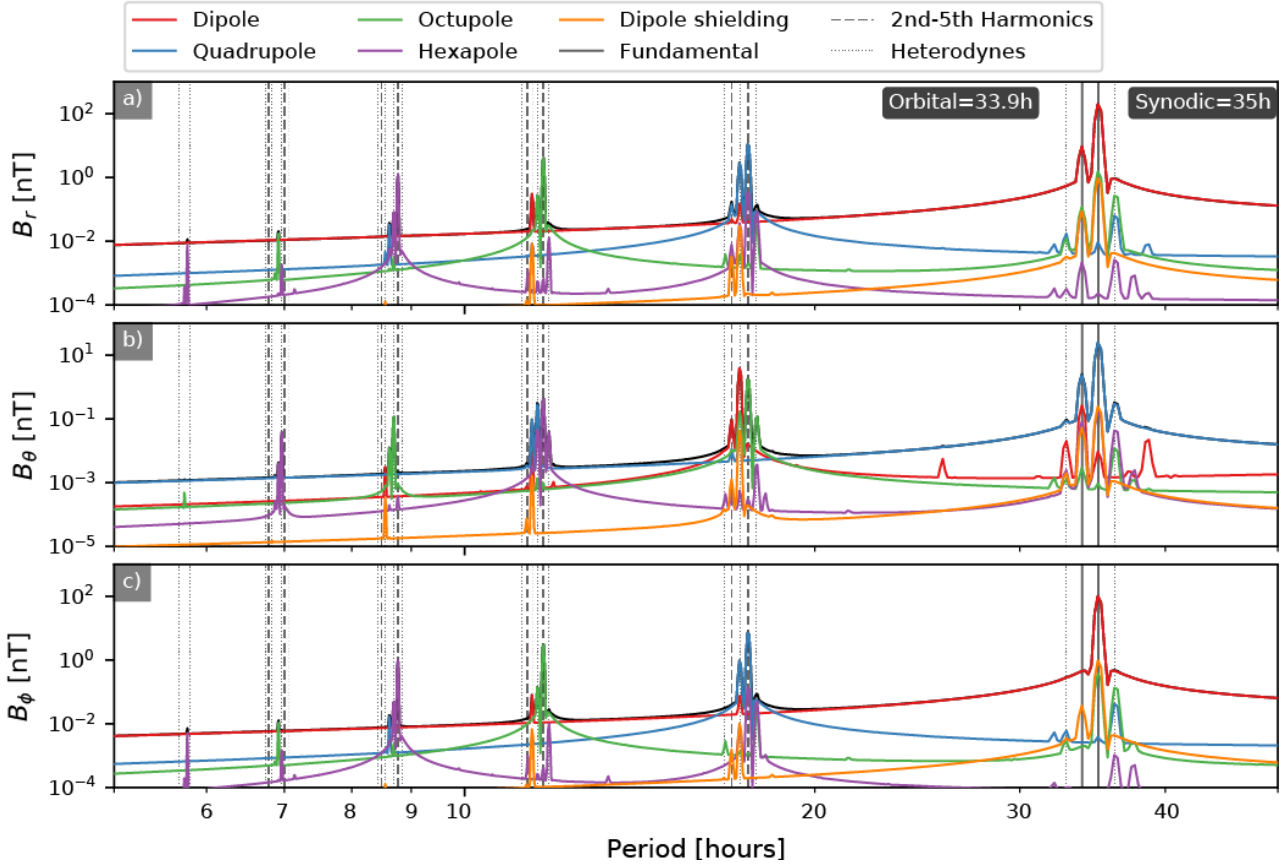
415



416
 417 Figure 10: Amplitude spectrum for Titania near equinox. The spectrum is similar to that near solstice but with larger
 418 amplitude heterodynes at equinox. The four terms in the internal field (dipole, quadrupole, octupole, hexapole) and
 419 the magnetopause field (dipole shielding) are shown with the total in black. Orbital and synodic periods are indicated
 420 by solid vertical grey lines and their higher harmonics by heavy grey dashed lines. Dotted lines indicate a range of the
 421 most significant heterodynes.

422

423 For contrast, Figure 11 shows the amplitude spectrum at Miranda. As the orbital and synodic periods are very close
 424 together we show the spectrum over a smaller range of periods. Similar to the spectrum at Titania, the heterodynes
 425 produce a great deal of fine structure but, in contrast, this fine structure is greatly compressed due to the proximity of
 426 the orbital and synodic periods and is compressed into packets near the harmonics of the orbital and synodic periods.
 427 Many of the peaks are under-resolved or compressed together and any further work on the inducing signals at Miranda
 428 should use a larger sampling frequency to enable the resolution of this fine structure. One significant difference
 429 between Miranda and Titania is the importance of the higher degree structure in Uranus' internal field. The
 430 quadrupole, octupole and hexapole all present significant contributions to the inducing field and the magnetopause
 431 field is around two orders of magnitude smaller than these contributions.



432

433 Figure 11: Amplitude spectrum for Miranda near solstice in the same format as Figure 10 but with a reduced range of
 434 periods.

435 3.4 Primary field amplitudes

436 To extract the primary field amplitudes we fit the linear decomposition in equation (2) to the time series rather than
 437 determining the amplitudes from the spectra. For each harmonic, m , we represent the primary field as $\mathbf{B}_m =$
 438 $\mathbf{B}_q \cos \omega_m t + \mathbf{B}_s \sin \omega_m t$, where \mathbf{B}_q and \mathbf{B}_s are constant real-valued vectors that encode the amplitude, phase and
 439 polarisation of the primary field (e.g., the hodogram structure in Figures 7 and 8) as $\mathbf{B}_q =$
 440 $(B_{xq} \cos \phi_{xq}, B_{yq} \cos \phi_{yq}, B_{zq} \cos \phi_{zq})$ and $\mathbf{B}_s = (B_{xs} \cos \phi_{xs}, B_{ys} \cos \phi_{ys}, B_{zs} \cos \phi_{zs})$. These harmonics, plus a
 441 constant term, were fitted to the synthetic time series using a linear least squares matrix inversion using
 442 `scipy.optimize.lsqr_linear` without bounds. For n samples and p harmonics, the matrix problem for the B_x
 443 component can be written as:

$$444 \begin{bmatrix} B_x(t_0) \\ B_x(t_1) \\ \vdots \\ B_x(t_{n-1}) \end{bmatrix} = \begin{bmatrix} 1 & \cos \omega_1 t_0 & \sin \omega_1 t_0 & \dots & \cos \omega_p t_0 & \sin \omega_p t_0 \\ 1 & \cos \omega_1 t_1 & \sin \omega_1 t_1 & \dots & \cos \omega_p t_1 & \sin \omega_p t_1 \\ \vdots & \vdots & \vdots & \vdots & \vdots & \vdots \\ 1 & \cos \omega_1 t_{n-1} & \sin \omega_1 t_{n-1} & \dots & \cos \omega_p t_{n-1} & \sin \omega_p t_{n-1} \end{bmatrix} \begin{bmatrix} C \\ B_{xq,1} \cos \phi_{xq,1} \\ B_{xs,1} \sin \phi_{xs,1} \\ \vdots \\ B_{xq,p} \cos \phi_{xq,p} \\ B_{xs,p} \sin \phi_{xs,p} \end{bmatrix} \quad (9)$$

445

446 The selection of harmonics was performed algorithmically. Prior to the fit, a list of trial periods was constructed from
447 the orbital, synodic and Uranus rotation periods, their higher harmonics, and heterodynes up to a maximum harmonic
448 degree of 8. At each step of the fitting a period was removed from this list and added to a list of periods. The matrix
449 (9) is constructed for each field component and the matrix inverted to provide a list of coefficients. The residuals are
450 calculated and from these the root-mean-square error, the maximum relative (to the peak in that component) error,
451 and the reduced χ^2 . The added period is only retained if the quality of the fit is improved, defined by the root-mean-
452 square, reduced χ^2 , or maximum relative error decreasing by a factor of $1-10^{-7}$, for all three field components.

453 Table 1 contains the amplitudes and driving periods for Titania, at solstice and equinox, and Oberon at solstice. Driving
454 periods were only included that were within a factor of 10^{-3} of the maximum amplitude for that field component. The
455 identified source of the driving harmonic is listed in the right-hand column. For some harmonics there are multiple
456 physical sources that contribute to that harmonic and we list all the contributors up to 90% of the amplitude of that
457 harmonic; for example, if the dipole can explain 89% of a harmonic then we also list the next most important
458 contribution to get to at least 90%.

459

B	0.058	209	0.0632	209		MP	Orbital
ϕ							

460

461 Table 1: Amplitudes and periods of the inducing field at Titania near equinox and solstice, and Oberon near solstice.

462 Amplitudes are given to 3 s.f. and periods to 4 s.f.. The right hand columns indicate the source of the signal and the

463 nature of the inducing period where Uranus is the rotation period of Uranus, Orbital indicates the orbital period of the

464 satellite, and Synodic indicates the synodic period of the satellite. H- and H+ indicate a heterodyne between the two

465 listed periods, e.g., H+ Orbital (2nd) / Synodic indicates a positive heterodyne between the 2nd harmonic of the orbital

466 period and the synodic period, and MP indicates the field of the magnetopause currents.

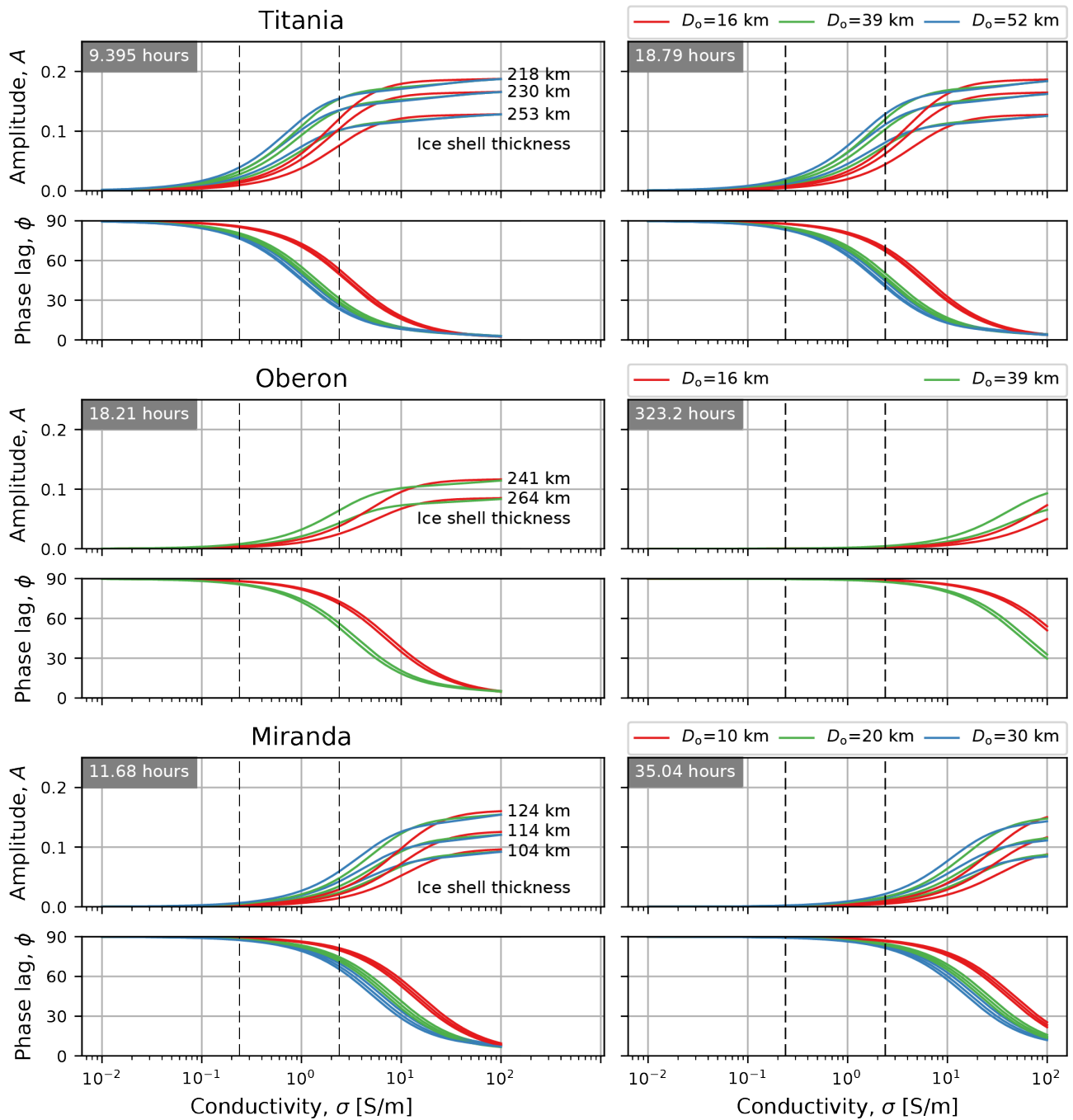
468 **4. Detectability of an induced field: Implications for future missions**

469 **4.1 Amplitude and phase**

470 Figure 12 shows the amplitude and phase, from equations (4) and (5), of the induced response at Titania, Oberon and
471 Miranda for representative driving periods and as a function of ocean conductivity. The conductivity spans four orders
472 of magnitude to explore the parameter space and to highlight the solutions, although it is important to highlight that
473 conductivity at the upper end of the range is unrealistic as salts reach saturation at ~ 6 S/m for MgSO_4 and ~ 18 S/m for
474 NaCl (Hand and Chyba, 2007). Although the 9.395 hour second harmonic of the synodic period at Titania is not a high
475 amplitude signal, this is included to provide contrast with the signals near the synodic period. The amplitude of the
476 induced response is typically below 0.2 and is very different to the scenario at Europa with an amplitude of 0.97 ± 0.02
477 (Schilling et al., 2004). This much smaller amplitude is principally due to the thick ice shell overlying the ocean; thinner
478 ice shells of around 50 km in depth produce larger amplitudes near 0.8. Although the Hussman, Sohl and Spohn (2006)
479 models do not include solutions with such thin ice shells, they also fail to do so for Enceladus and it has been shown via
480 Cassini observations of Enceladus' gravity field that there is a relatively thin ice shell overlying an ocean (Čadek et al.
481 (2016). The models for Europa also contain much thicker ice shells than constraints from observations (e.g., Hand and
482 Chyba, 2007). Thus, thin ice shells may also be common at the uranian icy satellites but we restrict our focus to the
483 model of Hussman, Sohl and Spohn (2006) as physically motivated ice shell thicknesses. In the following examination
484 we explore two conductivity limits, a) 2.75 S/m, consistent with the conductivity of Earth's oceans and requiring 96.8 g
485 MgSO_4 per kg of H_2O in the ocean (Hand and Chyba, 2007), and b) 0.275 S/m, requiring only 4g MgSO_4 per kg of H_2O .

486 At Titania, the amplitude of the induced field at 18.79 hours ranges from 0.43 to 1.2 nT for the different ocean
487 configurations, and 0.014 to 0.026 nT at 9.395 hours ($\sim 3\%$ of the response at the synodic period). The heterodynes
488 near the synodic period provide relatively strong responses around 10% of those at the synodic period, however their
489 phases are lagged by more than 15° from the response at the synodic period. At a conductivity of 0.275 S/m the
490 response at 18.79 hours ranges between 10 and 17% of the values at the higher conductivity for the three ocean
491 configurations. However, crucially, the phase is further lagged between 20° and 46° suggesting the possibility to
492 distinguish between ocean depth and conductivity from future observations.

493 By way of contrast, at Miranda the amplitudes (Figure 12) are lower but the primary field is much higher indicating the
494 possibility for detecting an ocean. The clear separation of synodic periods provides more driving periods. At the
495 synodic period of 35.04 hours the amplitudes are between 2.0 and 8.5 nT for 10 to 30 km oceans, and at the second
496 harmonic of 17.52 hours the amplitude is 0.27 to 1.1 nT. The difference in phase lag varies by almost 20° between the
497 first and third harmonics of the synodic period for the 30 km ocean, but only 6° for the 10 km thick ocean. At the lower
498 conductivity the responses are between 0.2 to 0.86 nT, although the 10 km ocean cannot be accurately modelled by an
499 induced dipole at the lower conductivity (explored further in the discussion and conclusions).



500

501 Figure 12: The amplitude and phase lag of the induced response at Titania (top), Oberon (middle) and Miranda
 502 (bottom) for two representative driving periods. Each panel shows three separate ocean depths and ice shell
 503 thicknesses broadly following the solutions of Hussman et al. (2006), except for Miranda which is more speculative.
 504 The vertical dashed lines indicate solutions for conductivities of 0.275 and 2.75 S/m.

505

506 4.2 Synthetic flyby

507 For a more practical assessment of the visibility of an ocean we examine the magnetic field perturbation from a flyby of
 508 Titania. To estimate the effect of random and systematic errors on the measurements we constructed a simple forward

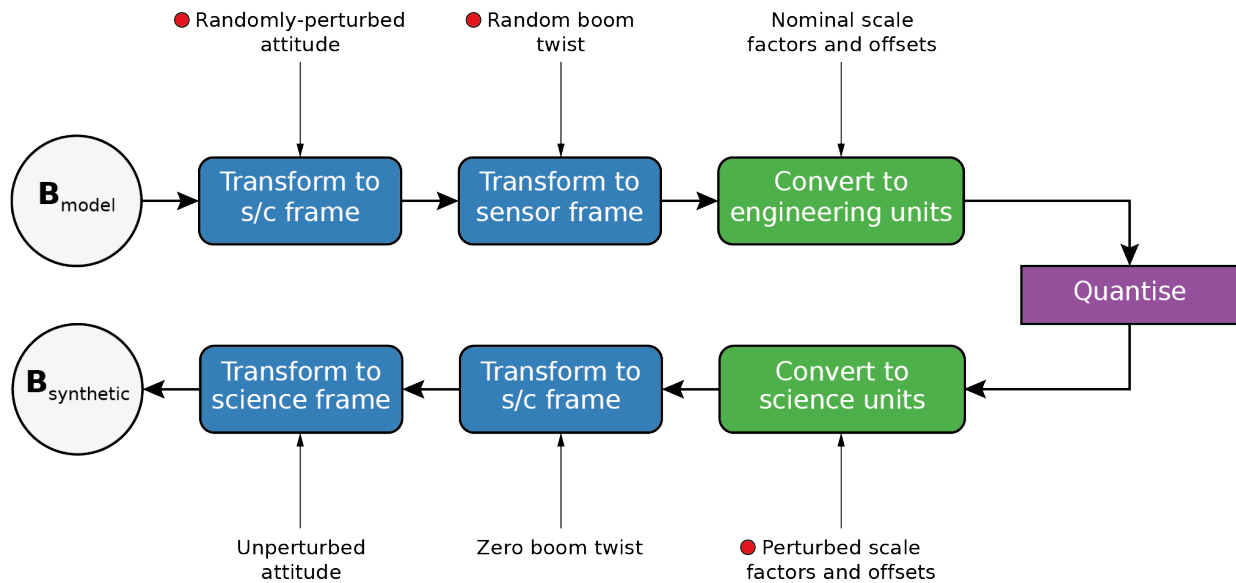
509 model of the Voyager magnetometer. We incorporate the transformation from the sensor to spacecraft frame,
510 $\mathbf{M}_{\text{sensor-sc}}$, spacecraft to geophysical frame, $\mathbf{M}_{\text{sc-geo}}$, and incorporated scale factors, \mathbf{k} , and offsets, \mathbf{z} , according to
511 equation (10) (after Acuña, 2002) to convert from engineering (measured) units, \mathbf{V} , to field strength, \mathbf{B} .

$$512 \quad \mathbf{B} = \mathbf{k}(\mathbf{V} - \mathbf{z})\mathbf{M}_{\text{sensor-sc}}\mathbf{M}_{\text{sc-geo}} \quad (10)$$

513 In a real set of spacecraft observations the transformations $\mathbf{M}_{\text{sensor-sc}}$ and $\mathbf{M}_{\text{sc-geo}}$ contain errors due to twisting and
514 bending motions of the boom away from some calibrated alignment and a finite knowledge and control of the
515 spacecraft attitude. The scale factors and offsets are also subject to uncertainty. These can all be controlled to some
516 degree through calibration but systematic and random errors persist. The data in engineering units are also quantised
517 into a finite number of bits thus generating some quantisation noise. In the case of Voyager the data are quantised into
518 12 bits, although some of these bits are used for 'guard bands' at the upper and lower extrema of each sensitivity
519 range (Behannon et al., 1977; Berdichevsky, 2009) reducing the available bits by five for Voyager. To assess the impact
520 of these uncertainties and quantisation our forward model takes the modelled magnetic field during a flyby, transforms
521 the modelled data into quantised engineering units via equation (10), and then reinverts the data to produce a
522 synthetic timeseries. This is schematically illustrated in Figure 13.

523 The attitude of the spacecraft was specified with some constant axial tilt and a time-varying roll rate to give some
524 constant changing attitude with respect to the ambient field. Both angles were perturbed with normally-distributed
525 angles with a standard deviation of 0.035° to give a maximum RMS error of around 0.05° thus simulating finite
526 knowledge/control of the spacecraft attitude. For simplicity, the error on the alignment of the boom was simulated by
527 twisting the boom around its long axis and we did not consider bending of the boom. This was effected by generating a
528 set of random boom twist angles, equally-spaced in time, that were converted into a continuous boom twist angle via
529 cubic interpolation. The random twist angles were generated from a normal distribution with a standard deviation of
530 0.25° to give a twist amplitude less than 1° (Miller, 1979). Small errors in the offsets and scale factors were introduced
531 by perturbing the offsets by ± 6 counts (Berdichevsky, 2009) and the scale factors were scaled by a normally distributed
532 factor $\sim N(1, 0.01)$ to simulate an error of up to around 4%, e.g., instead of 0.005 nT/count, for example, the scale
533 might be ~ 0.0048 or ~ 0.0052 nT/count. No attempt is made to specifically emulate the Voyager magnetometer in great
534 detail – just as a template for a reasonable magnetometer that might measure the fields at Uranus.

535



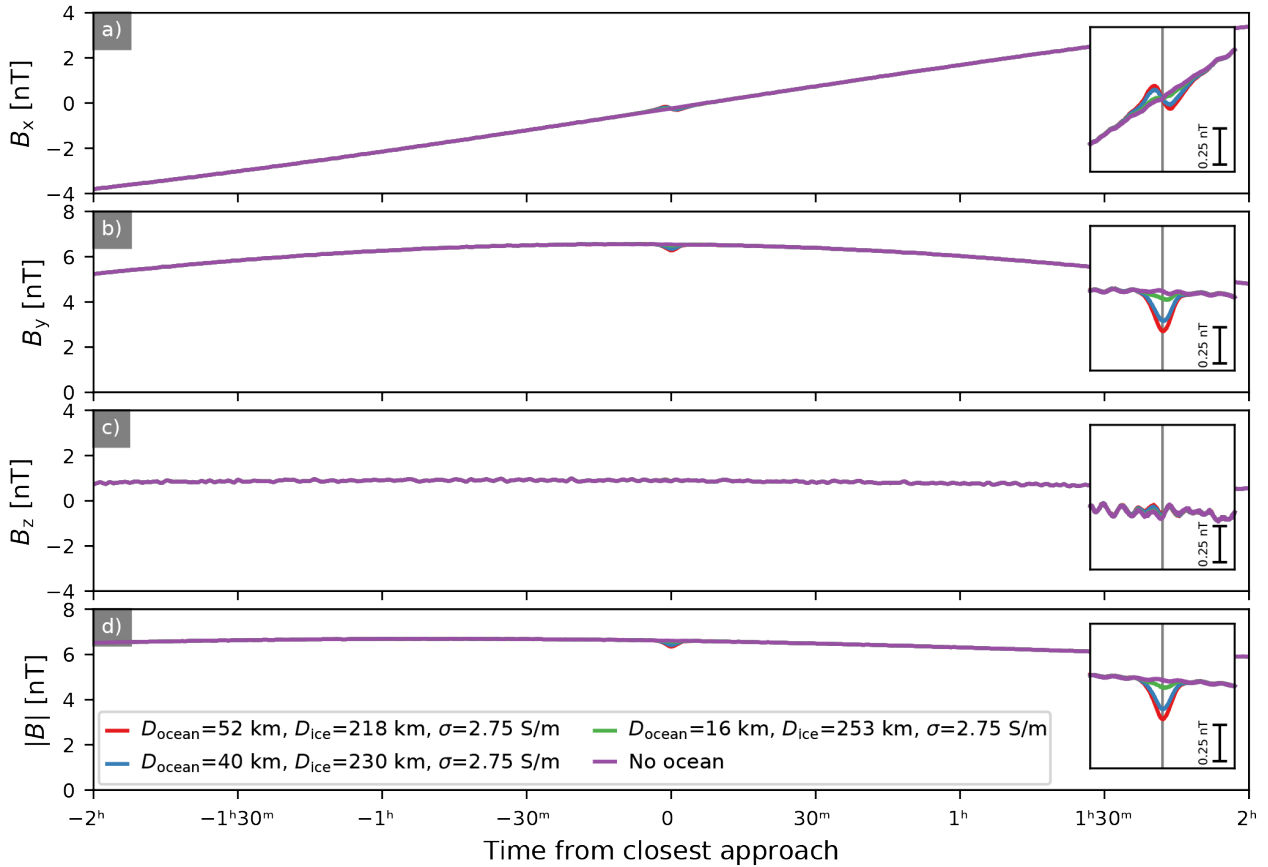
536

537 Figure 13: Schematic diagram showing how the forward model is used to generate a synthetic time series from the
 538 modelled magnetic field. Blue boxes indicate rotations between reference frames, green indicate conversions involving
 539 scale factors and offsets, the purple box indicates the quantisation procedure. Data introduced into this pipeline are
 540 indicated to the top and bottom, and red circles indicate where errors are introduced.

541

542 Each primary harmonic was calculated and used to determine the secondary field for a conductivity of 2.75 S/m. The
 543 total field was calculated and the constant terms added to generate the ideal field which was then subjected to the
 544 transformations described above. We computed the field along a flyby trajectory with a closest approach altitude of
 545 200 km at a 13° inclination and a flyby speed of 4.5 km/s consistent with the orbital tour presented in the Ice Giants
 546 Pre-Decadal Survey Mission Study Report (Hofstadter, Simon et al., 2017). Figure 14 shows the results of our synthetic
 547 time series. The small amplitude fluctuations in the B_z component are due to the simulated attitude and boom twisting
 548 uncertainties. Quantisation noise is generally small and unimportant on this scale and in this magnetometer range.
 549 Ocean thicknesses of 40 and 52 km should be readily detectable from the bipolar signature in B_x and negative peak in
 550 B_y . The perturbation in B_z is generally masked by orientation errors with magnitudes of around 0.1 nT. Ocean
 551 thicknesses of 16 km with a conductivity of 2.75 S/m present a more marginal case for detection from a 200 km altitude
 552 flyby, especially if there is a significant plasma interaction that may mask the induction signature. However, it is
 553 important to stress that we consider this as a conservative examination of the errors and careful calibration work could
 554 mitigate the errors we have considered. It also provides input for constraints required on a future magnetometer
 555 instrument and spacecraft platform.

556



557

558 Figure 14: Synthetic time series for a flyby of Titania in satellite-centred interaction coordinates: y is orientated
 559 towards Uranus from the satellite, x along the orbit of the satellite, and z perpendicular to the orbit plane. The inset
 560 shows a period ± 15 minutes from closest approach on a smaller scale. The induced perturbations due to the 39 and 52
 561 km ocean models are relatively clearly identified by the perturbation from the 16 km ocean is relatively small.

562 5. Discussion and conclusions

563 In this paper we have explored the possibility of detecting subsurface oceans at the uranian icy satellites, focusing on
 564 the outer two satellites, Titania and Oberon, as thermal and structural models have identified these as candidates for
 565 hosting subsurface oceans. An analytical model for the uranian magnetospheric magnetic field was constructed and
 566 used to generate magnetic field time series at the orbits of the five main satellites. These time series were subjected to
 567 a spectral analysis to identify the periods of driving signals and their amplitudes were determined via fitting a model
 568 harmonic time series. The amplitude of the induced field was calculated at the identified periods to examine the
 569 strength of a possible induced response. We found significant periodic signals near the synodic and orbital periods, and
 570 their higher harmonics, alongside a rich spectrum of heterodynes particularly associated with the magnetopause field.

571 The heterodynes were found to be a persistent feature in the magnetopause field due to a mixing of the synodic period
 572 with the orbital period and its harmonics. This was interpreted as the product of two effects:

- 573 • Orbital period: A satellite would experience a changing magnetopause field as it orbited within an
574 asymmetrical magnetospheric cavity.
- 575 • Diurnal period (+harmonics): As Uranus rotates the solar wind attack angle varies in a (generally) non-
576 sinusoidal fashion (e.g., Figure 3) and therefore the magnetopause field has a diurnal periodicity plus higher
577 order harmonics due to the non-sinusoidal variation in the attack angle.

578 We found that the identified induced field amplitudes at Titania can vary by a factor of around three between equinox
579 and solstice, due to the variation of both satellite orbit geometry relative to the magnetopause and the solar wind
580 attack angle with season, although this variation in amplitude was mostly restricted to the rich spectrum of
581 heterodynes. The spectrum was found to be generally richer at equinox but contained many closely spaced spectral
582 lines around the synodic period. It remains to be seen if these could be separated and used to constrain a subsurface
583 ocean. It is worthwhile commenting that there is some evidence for similar fine structure at Ganymede, e.g. via an
584 inspection of Figure 4 in Seufert et al., (2011) although the amplitudes are smaller as expected for a satellite much
585 deeper within the magnetosphere (up to around 50% of the magnetopause subsolar distance) than Titania and Oberon.

586 The major seasonal effect is the proximity of Oberon to the magnetopause. For a period of around ± 7 years centred on
587 2030 Oberon should remain inside the magnetosphere and the results from Table 1 apply. After that time, e.g., for
588 missions arriving later in the 2030s or in the 2040s, it may be possible to detect an ocean, but only from signals near the
589 synodic period and where the satellite has been inside the magnetosphere for a significant period while the eddy
590 currents establish themselves. This places clear constraints on flyby locations and would require a flyby to be timed for
591 after Oberon had left the vicinity of the dayside magnetosphere (moving towards the nightside) and preferably just
592 before it re-emerges into the dayside from the nightside magnetosphere.

593 These driving periods were combined with a model for the induction response and we showed that induced signatures
594 should be detectable and this was confirmed with a magnetometer forward model and synthetic time series from a
595 Titania flyby. We found that ocean thicknesses of 40 and 52 km should be readily detectable from a flyby with a 200
596 km altitude closest approach, although a 16 km thick ocean was at the limit of detectability. This analysis demonstrated
597 that a 200 km altitude flyby would be acceptable, but would limit ocean depth/conductivity/ice shell ranges and so
598 lower altitude flybys are strongly recommended. Given the weakness of some signals, this also demonstrates that
599 maintaining an AC spacecraft magnetic field below 0.1 nT (preferably below 0.01 nT) at the magnetometer would be
600 advantageous in our ability to resolve less conducting, thinner, and or deeper oceans; although more accurate
601 constraints require further study. It is important to highlight that this work has been guided by the work of Hussmann
602 et al. (2006) and thinner overlying ice shells would result in stronger induced fields and thus would be more readily
603 detectable than the somewhat thicker ice shells predicted by Hussmann.

604 We used an induced dipole model to represent the response of a subsurface ocean. This model is valid when the ocean
605 depth is much greater than the electromagnetic skin depth, $\delta = \sqrt{2/\sigma\mu_0\omega}$ (e.g., Khurana et al., 1998). For Titania this
606 is almost always satisfied for the 39 and 52 km thick oceans, over a wide range of conductivities above 0.1 S/m. The
607 exception to this is that the 209 hour orbital period signal can only be analysed for conductivities above 1 S/m with this
608 model. The thinner 16 km ocean requires higher conductivities > 1 S/m for the main driving periods under this model.

609 A similar set of restrictions also apply to Oberon. At Miranda the model is only valid above around 3 S/m for the 10 km
610 ocean case, but is less stringent for the 20 and 30 km ocean cases.

611 Attempting to model fields due to a plasma interaction was deemed beyond the scope of this work and requires further
612 analysis. From a stellar occultation in 2001, Widemann et al. (2009) placed an upper limit of 9-17 nbar on the surface
613 pressure of a CO atmosphere with temperatures of 60-80 K respectively, far below the surface pressure at Triton, Pluto
614 and Europa. Hence, due to Uranus' large heliocentric distance and relatively low densities of sufficiently high
615 temperature electrons to drive electron impact ionisation (e.g., Sittler et al., 1987), there may be a negligible
616 interaction between the plasma in the magnetosphere and only a tenuous ionosphere. Therefore the interaction may
617 consist of a downstream plasma wake with Alfvén wings. However, the surface pressure may well be seasonally
618 dependent and one shouldn't rule out plume-like activity such as that found at Enceladus. Regardless, although the
619 plasma beta is generally low, ~ 1 near the plasma sheet (Behannon et al., 1987), the field strength is also lower and so
620 plasma interaction currents and therefore their field, may be higher in order to balance the forces associated with the
621 plasma interaction. The location of Titania and Oberon close to the magnetotail may introduce additional influences
622 due to magnetospheric dynamics.

623 We specifically excluded solar wind variability in order to focus on the asymmetrical and seasonal drivers, but future
624 work should incorporate this source of variability. We have begun to explore this effect and have identified drivers at
625 the solar periodicity with amplitudes of order 0.1 nT at Titania and Oberon.

626 In summary:

- 627 1. From our simple model of Uranus' magnetospheric magnetic field there are a rich spectrum of magnetic field
628 periodicities at the natural satellites of Uranus. The more distant satellites show considerable seasonally-
629 dependent fine structure associated with the geometry of the solar wind-magnetosphere interaction and
630 orientation of the satellite orbital plane, whereas the inner satellites show stronger signals from the
631 asymmetrical internal field.
- 632 2. From models of expected subsurface ocean structure (Hussmann, Sohl and Spohn, 2006), an induction model,
633 and our model of the inducing field, the amplitude of the modelled induced response is typically below 0.2 and
634 is very different to Europa with an amplitude of 0.97 ± 0.02 (Schilling et al., 2004). This much smaller amplitude
635 is principally due to the thick ice shell overlying the ocean and thinner ice shells produce larger responses of
636 order 0.8. It is worth remarking that the models of Hussmann, Sohl and Spohn (2006) also fail to reproduce
637 the thin shell at Enceladus as inferred from Cassini observations (Čadek et al. (2016).
- 638 3. Thick ocean models at Titania are detectable from a 200 km altitude flyby, but a 16 km thick ocean is at the
639 limit of detectability. Detection of oceans at Oberon is complicated by the proximity of Oberon to the
640 magnetopause and so flybys should be designed to encounter Oberon on the nightside of Uranus near
641 equinox.
- 642 4. Further work should explore i) additional periodicities driven by solar wind variations; ii) the relative
643 importance of plasma interaction currents; and iii) the inclusion of tail current systems.

644

645 **Acknowledgements**

646 CSA was funded by a Royal Society Research Fellowship and the STFC Consolidated Grant to Lancaster University.

647 Colours from www.ColorBrewer2.org by Cynthia A. Brewer, Geography, Pennsylvania State University.

648 **References**

649 Acton, C.H. (1996) Ancillary Data Services of NASA's Navigation and Ancillary Information Facility. *Planet. Sp. Sci.*, 44(1),

650 65-70.

651 Acuña, M. H. (2002). Space-based magnetometers. *Review of Scientific Instruments*, 73(11), 3717.

652 <https://doi.org/10.1063/1.1510570>

653 Anderson, J.D., G. Schubert, R.A. Jacobson, E.L. Lau, W.B. Moore, W.L. Sjogren (1998) Europa's differentiated internal

654 structure: Inferences from four Galileo encounters. *Science* 281, pp. 2019-2022.

655 Annex, A.M., B. Pearson, B. Seignovert, B.T. Carcich, H. Eichhorn, J.A. Mapel, J.L. Freiherr von Forstner, J. McAuliffe, J.

656 Diaz del Rio, K.L. Berry, K.-M. Aye, M. Stefko, M. de Val-Borro, S. Kulumani, S.-y. Murakami (2020) *SpiceyPy: a Pythonic*

657 *Wrapper for the SPICE Toolkit*. *J. Open Source Software* 5(45), 2050, doi:10.21105/joss.02050.

658 Arridge, C.S., C.J. Martin (2018) *Current Sheets at the Giant Planets*, in, *Electric Currents in Geospace and Beyond*, ed. A.

659 Keiling, O. Marghitu, M. Wheatland. *Geophysical Monograph Series*. Wiley.

660 Arridge, C.S., C. Paty (in press).

661 Arridge, C.S., J.A. Wiggs (2019) *Ikuchi: 3D Views of Solar System Magnetospheres*. Zenodo

662 doi:10.5281/Zenodo.3451443.

663 Behannon, K.W., M.H. Acuña, L.F. Burlaga, R.P. Lepping, N.F. Ness, F.M. Neubauer (1977) *Magnetic Field Experiment for*

664 *Voyagers 1 and 2*. *Space Sci. Rev.* 21(3), pp. 235-257, doi:10.1007/BF00211541.

665 Behannon, K.W., R.P. Lepping, E.C. Sittler, Jr., N.F. Ness, B.H. Mauk, S.M. Krimigis, R.L. McNutt, Jr. (1987) *The*

666 *magnetotail of Uranus*. *J. Geophys. Res.* 92(A13), 15354-15366.

667 Berdichevsky, D.B. (2009) *Voyager Mission, Detailed processing of weak magnetic fields; I - Constraints to the*

668 *uncertainties of the calibrated magnetic field signal in the Voyager missions*. Available at

669 https://vgrmag.gsfc.nasa.gov/Berdichevsky-VOY_sensor_opu090518.pdf.

670 Čadek, O., G. Tobie, T. Van Hoolst, M. Massé, G. Choblet, A. Lefèvre, G. Mitri, R.-M. Baland, M. Běhouňková, O.

671 Bourgeois, A. Trinh (2016) *Enceladus's internal ocean and ice shell constrained from Cassini gravity, shape, and libration*

672 *data*. *Geophys. Res. Lett.*, 43, 5653– 5660, doi:10.1002/2016GL068634. Chyba, C.F., K.P. Hand, P.J. Thomas (2021) *Icarus*

673 360, 114360, doi:10.1016/j.icarus.2021.114360.

674 Colburn, D. S., R.T. Reynolds (1985). Electrolytic currents in Europa. *Icarus*, 63(1), 39–44, doi:10.1016/0019-
675 1035(85)90019-3.

676 Connerney, J.E.P., M.H. Acuña, N.F. Ness (1987) The Magnetic Field of Uranus. *J. Geophys. Res.* 92(A13), 15329-15336.

677 Croft, S.K. and L.A. Soderblom (1991) Geology of the Uranian satellites. In *Uranus*, ed. J.T. Bergstrahl, E.D. Miner and
678 M.S. Matthews. University of Arizona Press.

679 Hand, K.P. and C.F. Chyba (2007) Empirical constraints on the salinity of the european ocean and implications for a thin
680 ice shell. *Icarus* 189, 424-438, doi: 10.1016/j.icarus.2007.02.002.

681 Herbert, F. (2009) Aurora and magnetic field of Uranus. *J. Geophys. Res.* 114, A11206, doi:10.1029/2009JA014394.

682 Hofstadter, M., A. Simon et al. (2017), Ice Giants Pre-Decadal Survey Mission Study Report. Published by Planetary
683 Science Division Science Mission Directorate, NASA. Report JPL D-100520. Available at
684 https://www.lpi.usra.edu/icegiants/mission_study/Full-Report.pdf.

685 Hussmann, H., F. Sohl, T. Spohn (2006) Subsurface oceans and deep interiors of medium-sized outer planet satellites
686 and large trans-neptunian objects. *Icarus* 185, pp.258-273.

687 Jacobson, R.A. (2014a) The orbits of the uranian satellites and rings, the gravity field of the uranian system, and the
688 orientation of the pole of Uranus. *Astron. J.* 148(5), 76, doi:10.1088/0004-6256/148/5/76.

689 Jacobson, R.A. (2014b) URA112 Satellite Ephemeris available at
690 https://naif.jpl.nasa.gov/pub/naif/generic_kernels/spk/satellites/.

691 Kargel, J. S., and G.J. Consolmagno (1996). Magnetic fields and the detectability of brine oceans in Jupiter's icy satellites.
692 *Lunar Planet. Sci. Conf.*, XXVII, 643–644.

693 Khurana, K.K., M.G. Kivelson, D.J. Stevenson, G. Schubert, C.T. Russell, R.J. Walker, C. Polansky (1998) Induced
694 magnetic fields as evidence for subsurface oceans in Europa and Callisto. *Nature* 395, pp.777-780.

695 Khurana, K.K., M.G. Kivelson, K.P. Hand, C.T. Russell (2009) Electromagnetic induction from Europa's ocean and the
696 deep interior. In *Europa*, ed. R.T. Pappalardo, W.B. McKinnon, K.K. Khurana. University of Arizona Press.

697 Kivelson, M.G., K.K. Khurana, C. T Russell, M. Volwerk, R.J. Walker, C. Zimmer (2000) Galileo magnetometer
698 measurements strength the case for a subsurface ocean at Europa. *Science*, 289, pp.1340.

699 Lazcano, A., K.P. Hand (2012) Frontier or fiction. *Nature* 488, 160-161, doi:10.1038/488160a.

700 Lepping, R.P. (1994) Comparison of the field configurations of the magnetotails of Uranus and Neptune. *Planet. Space*
701 *Sci.* 42(10), pp. 847-857.

702 Miller, D.C. (1979) The Voyager Magnetometer Boom. 12th Aerospace Mechanisms Symposium NASA, Cal-Tech,
703 Lockheed. SP-2080. Published by NASA.

704 Nelder, J.A., R. Mead (1965) A simplex method for function minimization. *Computer Journal* 7(4), 308-313,
705 doi:10.1093/compjnl/7.4.308.

706 Oliphant, T.E. (2006) *A guide to NumPy*. Trelgol Publishing, USA.

707 Pappalardo, R.T., M.J.S. Belton, H.H. Breneman, M.H. Carr, C.R. Chapman, G.C. Collins, T. Denk, S. Fagents, P.E. Geissler,
708 B. Giese, R. Greeley, R. Greenberg, J.W. Head, P. Helfenstein, G. Hoppa, S.D. Kadel, K.P. Klaasen, J.E. Klemaszewski, K.
709 Magee, A.S. McEwen, J.M. Moore, W.B. Moore, G. Neukum, C.B. Phillips, L.M. Prockter, G. Schubert, D.A. Senske, R.J.
710 Sullivan, B.R. Tufts, E.P. Turtle, R. Wagner, K.K. Williams (1999) Does Europa have a subsurface ocean? Evaluation of the
711 geological evidence. *J. Geophys. Res.* 104(E10), pp.24015-24055, doi:10.1029/1998JE000628.

712 Saur, J., F.M. Neubauer, K.-H. Glassmeier (2010) Induced magnetic fields in solar system bodies. *Space Sci. Rev.* 152,
713 391-421.

714 Schilling, N., K.K. Khurana, M.G. Kivelson (2004) Limits on an intrinsic dipole moment in Europa. *J. Geophys. Res.*, 109,
715 E05006, doi:10.1029/2003JE002166.

716 Schilling, N., F.M. Neubauer, J. Saur (2007) Time-varying interaction of Europa with the jovian magnetosphere:
717 Constraints on the conductivity of Europa's subsurface ocean. *Icarus* 192, pp.41-55.

718 Schulz, M., M.C. McNab (1996) Source-surface modelling of planetary magnetospheres. *J. Geophys. Res.* 101(A3), 5095-
719 5118.

720 Seufert, M., J. Saur, F.M. Neubauer (2011) Multi-frequency electromagnetic sounding of the Galilean moons. *Icarus* 214,
721 477-494, doi:10.1016/j.icarus.2011.03.017.

722 Shue, J.-H., J.K. Chao, H.C. Fu, C.T. Russell, P. Song, K.K. Khurana, H.J. Singer (1997) A new functional form to study the
723 solar wind control of the magnetopause size and shape. *J. Geophys. Res. Space Physics*, 102(A5), 9497-9511, doi:
724 10.1029/97JA00196.

725 Sittler, E.C., K.W. Ogilvie and R. Selesnick (1987) Survey of Electrons in the Uranian Magnetosphere: Voyager 2
726 Observations. *J. Geophys. Res.* 92(A13), pp.15263-15281.

727 Smith, E. J., L. Davis, D.E. Jones, P.J. Coleman, D.S. Colburn, P. Dyal, C.P. Sonett, and A.M.A. Frandsen (1974) The
728 planetary magnetic field and magnetosphere of Jupiter: Pioneer 10. *J. Geophys. Res.*, 79(25), 3501– 3513,
729 doi:10.1029/JA079i025p03501.

730 P.C. Thomas, P.C., R. Tajeddine, M.S. Tiscareno, A. Burns, J. Joseph, T.J. Lored, P. Helfenstein, C. Porco (2016)
731 Enceladus's measured physical libration requires a global subsurface ocean. *Icarus*, 264, 37-47,
732 doi:10.1016/j.icarus.2015.08.037.

733 Tóth, G., D. Kovács, K.C. Hansen, T.I. Gombosi (2004) Three-dimensional MHD simulations of the magnetosphere of
734 Uranus. *J. Geophys. Res.*, 109, A11210, doi:10.1029/2004JA010406.

735 Tsyganenko, N.A. (2002) A model of the near magnetosphere with a dawn-dusk asymmetry. 1. Mathematical structure.
736 J. Geophys. Res. 107(A8), doi:10.1029/2001JA000219.

737 Virtanen, P., R. Gommers, T.E. Oliphant, M. Haberland, T. Reddy, D. Cournapeau, E. Burovski, P. Peterson, W.
738 Weckesser, J. Bright, S.J. van der Walt, M. Brett, J. Wilson, K.J. Millman, N. Mayorov, A.R.J. Nelson, E. Jones, R. Kern, E.
739 Larson, C.J. Carey, Í. Polat, Y. Feng, E.W. Moore, J. VanderPlas, D. Laxalde, J. Perktold, R. Cimrman, I. Henriksen, E.A.
740 Quintero, C.R. Harris, A.M. Archibald, A.H. Ribeiro, F. Pedregosa, P. van Mulbregt, and SciPy 1.0 Contributors (in press)
741 SciPy 1.0: Fundamental Algorithms for Scientific Computing in Python. Nature Methods.

742 Welch, P. D. (1967) The use of Fast Fourier Transform for the estimation of power spectra: A method based on time
743 averaging over short, modified periodograms" IEEE Transactions on Audio and Electroacoustics, AU-15(2), 70–73,
744 doi:10.1109/TAU.1967.1161901.

745 Widemann et al. (2009), Titania's radius and an upper limit on its atmosphere from the September 8, 2001 stellar
746 occultation. Icarus 199, pp.458-476, doi:j.icarus.2008.09.011.

747 Zimmer, C., K.K. Khurana, M.G. Kivelson (2000) Subsurface oceans on Europa and Callisto: Constraints from Galileo
748 magnetometer observations. Icarus 147, 329-347.

749

750 **Appendix: Coefficients for dipole shielding field**

751 Units of a_{ij} , b_{ij} , c_{jl} , and d_{jl} are nT R_U and p_i , r_k , q_j , s_l are in units of R_U .

a_{00}	-0.5287296425170684
a_{01}	15.077691459563148
a_{02}	12.542608435251966
a_{10}	0.6790677915590768
a_{11}	0.528393529955896
a_{12}	5.187345418230727
a_{20}	7.588002567699361
a_{21}	-0.03895534291481634
a_{22}	-0.4309246786725432
b_{00}	-0.067659794456119
b_{01}	-0.26508462208523287
b_{02}	0.039048819175832444
b_{10}	0.003658445181747277
b_{11}	0.3800595786028047
b_{12}	-0.32854084061998434
b_{20}	0.07939129606739725

b_{21}	0.1722800052080468
b_{22}	0.010840039677544875
c_{00}	0.529043977091829
c_{01}	0.5531924779259334
c_{02}	2.795636187534518
c_{03}	4.1653942238057216
c_{10}	9.47249250384742
c_{11}	3.1398706541002945
c_{12}	0.5607158782730544
c_{13}	15.577086936808046
c_{20}	0.6801897898848649
c_{21}	8.167236925544106
c_{22}	8.544135882214677
c_{23}	-7.368520962970561
c_{30}	-0.000593516601684975
c_{31}	4.51881410634166

c_{32}	-2.629656639894243
c_{33}	0.07375174811174984
d_{00}	-0.01585995912343289
d_{01}	0.4876191637729948
d_{02}	-0.8042519008224641
d_{03}	0.31507763470267774
d_{10}	-0.27099432374589316
d_{11}	-1.3517952498602952
d_{12}	1.9871775394184894
d_{13}	0.5193719828782029
d_{20}	0.4998831443486746
d_{21}	0.0010817323978511068
d_{22}	4.23796706092375
d_{23}	-0.08589911614621044
d_{30}	-0.27901413410517384
d_{31}	1.9206493946310075

d_{32}	-3.329992459682197
d_{33}	-3.114276641196077
p_0	54.20597580715924
p_1	18.161591584063434
p_2	57.09281695782331
r_0	14.88166750097028
r_1	32.31074443198433
r_2	27.699339701283346
q_0	15.054040480643655
q_1	33.8559135376921
q_2	143.5427552567043
q_3	72.07887351621275
s_0	15.970961048424488
s_1	33.513749485292834
s_2	120.97202513997192
s_3	53.377584869814584

